Mountain wave turbulence in the presence of directional wind shear over the Rocky Mountains

Article

Published Version

Mountain-Wave Turbulence in the Presence of Directional Wind Shear over the Rocky Mountains

MARIA-VITTORIA GUARINO[a] AND MIGUEL A. C. TEIXEIRA

Department of Meteorology, University of Reading, Reading, United Kingdom

TEDDIE L. KELLER AND ROBERT D. SHARMAN

National Center for Atmospheric Research, Boulder, Colorado

(Manuscript received 26 April 2017, in final form 31 January 2018)

ABSTRACT

Mountain-wave turbulence in the presence of directional wind shear over the Rocky Mountains in Colorado is investigated. Pilot reports (PIREPs) are used to select cases in which moderate or severe turbulence encounters were reported in combination with significant directional wind shear in the upstream sounding from Grand Junction, Colorado (GJT). For a selected case, semi-idealized numerical simulations are carried out using the WRF-ARW atmospheric model, initialized with the GJT atmospheric sounding and a realistic but truncated orography profile. To isolate the role of directional wind shear in causing wave breaking, sensitivity tests are performed to exclude the variation of the atmospheric stability with height, the speed shear, and the mountain amplitude as dominant wave breaking mechanisms. Significant downwind transport of instabilities is detected in horizontal flow cross sections, resulting in mountain-wave-induced turbulence occurring at large horizontal distances from the first wave breaking point (and from the orography that generates the waves). The existence of an asymptotic wake, as predicted by Shutts for directional shear flows, is hypothesized to be responsible for this downwind transport. Critical levels induced by directional wind shear are further studied by taking 2D power spectra of the magnitude of the horizontal velocity perturbation field. In these spectra, a rotation of the most energetic wave modes with the background wind, as well as perpendicularity between the background wind vector and the wavenumber vector of those modes at critical levels, can be found, which is consistent with the mechanism expected to lead to wave breaking in directional shear flows.

1. Introduction

Mountain waves, also known as orographic gravity waves, result from stably stratified airflow over orography. These waves can break at different altitudes and influence the atmosphere both locally, by generating, for example, aviation-scale turbulence (Lilly 1978), and globally, by decelerating the general atmospheric circulation (Lilly and Kennedy 1973). Several studies have investigated the role of mountain-wave activity in a wide range of atmospheric processes taking place in the boundary layer (e.g., Durran 1990; Grubišić et al. 2015), in the midtroposphere (e.g., Jiang and Doyle 2004; Strauss et al. 2015), in the upper troposphere (e.g., Worthington 1998; Whiteway et al. 2003; McHugh and Sharman 2013), in the stratosphere (e.g., Carslaw et al. 1998; Eckermann et al. 2006), and in the mesosphere (e.g., Broutman et al. 2017).

Orographic gravity wave breaking in the mid- and upper troposphere can generate turbulence at aircraft-cruising altitudes. This is one of the known forms of clear-air turbulence (CAT), and it occurs, among other occasions, when large-amplitude waves approach critical levels, as this leads to a further increase of the wave amplitude. Critical levels correspond to singularities in the wave equation, where waves cease to propagate and break or are absorbed into the mean flow (Dörnbrack et al. 1995; Grubišić and Smolarkiewicz 1997), and above which the wave motion is no longer sustained, provided the Richardson number of the background flow is larger than about 1 (Booker and Bretherton 1967). For atmospheric flows where the wind direction

[a] Current affiliation: British Antarctic Survey, Cambridge, United Kingdom.

Corresponding author: Maria Vittoria Guarino, m.v.guarino@bas.ac.uk

DOI: 10.1175/JAS-D-17-0128.1

changes with height, the existence of critical levels is controlled by the relative orientations of the background wind vector and the horizontal wavenumber vector at each height. Broad (1995) and Shutts (1995) used linear theory to investigate the effects of directional wind shear on the gravity wave momentum fluxes, introducing the theoretical and mathematical framework for gravity wave drag in winds that turn with height.

Generally, mountain-wave critical levels exist when $\mathbf{U} \cdot \boldsymbol{\kappa}_H = u_0 k + v_0 l = 0$ [where $\mathbf{U} \equiv (u_0, v_0)$ is the background wind velocity and $\boldsymbol{\kappa}_H \equiv (k, l)$ is the horizontal wavenumber vector] (Teixeira 2014). For unidirectional shear flows [$u_0 = f(z)$, $v_0 = 0$, where f is an arbitrary function] or flows over two-dimensional ridges ($l = 0$), the definition of critical level reduces to $u_0 = 0$. For directional shear flows [$u_0 = f(z)$, $v_0 = g(z)$, where f and g are arbitrary functions] over idealized three-dimensional or complex (i.e., realistic) orographies (where $k \neq 0$ and $l \neq 0$), critical levels occur when the wind vector is perpendicular to the horizontal wavenumber vector, as expressed by the general condition presented above. This condition is difficult to assess from standard physical data, as the orientations of the wavenumber vectors can only be evaluated in Fourier space.

Previous theoretical and numerical studies investigating mountain waves in directional shear flows include Shutts (1998) and Shutts and Gadian (1999), who studied the structure of the mountain-wave field in the presence of directional wind shear; Teixeira et al. (2008), Teixeira and Miranda (2009), and Xu et al. (2012), who focused on the impact of directional wind shear on the mountain-wave momentum flux and, thus, on the gravity wave drag exerted on the atmosphere; and Guarino et al. (2016), who investigated the conditions for mountain-wave breaking in directional shear flows and their implications for CAT generation. All these studies considered idealized situations with a wind direction that turns continuously with height. This flow configuration is the simplest possible with directional wind shear and represents a prototype of more realistic flows.

We are aware of only two observational studies of this problem in the literature focused on real cases: Doyle and Jiang (2006) studied a wave breaking event in the presence of directional wind shear observed over the French Alps during the Mesoscale Alpine Programme (MAP), whereas Lane et al. (2009) studied aircraft turbulence encounters over Greenland and attributed the observed generation of flow instabilities to the interaction between mountain waves and directional critical levels.

In this paper, mountain-wave turbulence occurring in the presence of directional wind shear over the Rocky Mountains in Colorado is investigated. Numerical simulations for a selected turbulence encounter are performed using a semi-idealized approach, for which the WRF-ARW Model is used in an idealized configuration, but initialized with the real (albeit truncated) orography and a realistic atmospheric profile. A similar mixed approach, consisting of simulating a real event using a rather idealized model configuration, has been used in the past, for example, by Doyle et al. (2000), to study the 11 January 1972 Boulder, Colorado, windstorm and by Kirshbaum et al. (2007), to study orographic rainbands triggered by lee waves over the Oregon coastal range. This method allows us to retain the elements necessary to reproduce the mechanisms responsible for mountain-wave generation and breaking, while working in simplified conditions that facilitate physical interpretation. The simulation results are compared with theory and with idealized simulations, for a more comprehensive description and better physical understanding of the flow. The aim is to isolate the role of directional wind shear and determine its relevance in causing the observed turbulence event.

Because of its complexity, the wave breaking mechanism in directional shear flows is not currently taken into account for CAT forecasting purposes. Investigating its role in real turbulence encounters, as this paper aims to do, is part of the fundamental research needed to improve the forecasting methods of mountain-wave turbulence, which is currently one of the most poorly predicted forms of CAT (Gill and Stirling 2013). In fact, although mountain-wave turbulence is included in the forecasts provided by the London World Area Forecast Centre (WAFC), its prediction is still based on a method developed by Turner (1999), relying on diagnostics of the gravity wave drag from its parameterization in a global model (which itself does not accurately represent mountain-wave absorption by directional wind shear). A first attempt to account for mountain waves explicitly in CAT forecast was recently reported by Elvidge et al. (2017). The turbulence forecasting system Graphical Turbulence Guidance (GTG), described in Sharman and Pearson (2017), also contains several explicit mountain-wave turbulence (MWT) algorithms, but none consider the effect of directional wind shear. Furthermore, a predictor for mountain-wave CAT is absent in the forecast issued by the Washington WAFC (Gill 2014).

The remainder of the paper is organized as follows. In section 2, the mechanism leading to wave breaking in directional shear flows is discussed. In section 3, the methodology used to select the turbulence encounter investigated here and the setup of the numerical simulations is presented. In section 4, the simulation results are described and further discussed in the light of the sensitivity tests presented in the same section. In section 5, the main conclusions of the present study are summarized.

2. Wave breaking mechanism in directional shear flows

For a hydrostatic, adiabatic, three-dimensional, and frictionless flow without Earth's rotation, under the Boussinesq approximation, the wave equation from linear theory (also known as Taylor–Goldstein equation) takes the form (Nappo 2012):

$$\hat{w}'' + \left[\frac{(k^2+l^2)N_0^2}{(ku_0+lv_0)^2} - \frac{ku_0''+lv_0''}{ku_0+lv_0}\right]\hat{w} = 0, \tag{1}$$

where $\hat{w}$ is the Fourier transform of the vertical velocity, N_0 is the Brunt–Väisälä frequency of the background flow, and the primes denote differentiation with respect to z.

In vertically sheared background flows, the solution to (1) can be approximated as (Teixeira et al. 2004)

$$\hat{w}(k,l,z) = \hat{w}(k,l,0)\left|\frac{m(z=0)}{m(z)}\right|^{1/2} \exp\left[i\int_0^z m(z)\,dz\right], \tag{2}$$

where the bottom boundary condition is $\hat{w}(k, l, 0) = i(ku_0 + lv_0)\hat{h}(k, l)$, and $\hat{h}(k, l)$ is the Fourier transform of the terrain elevation $h(x, y)$. This corresponds to a first-order Wentzel–Kramers–Brillouin (WKB) approximation, where the vertical wavenumber m is defined as

$$m = \frac{N_0(k^2+l^2)^{1/2}}{ku_0+lv_0}, \tag{3}$$

as if N_0, u_0, and v_0 were constant, but where these quantities depend on z. Equations (2) and (3) are valid for any wavenumber vector (k, l) in the wave spectrum, as long as the background state variables N_0 and (u_0, v_0) vary sufficiently slowly with height. In addition, by mass conservation, it can be shown that the Fourier transforms of the horizontal velocity perturbations $\hat{u}'$ and $\hat{v}'$ are

$$\hat{u}'(k,l,z) = \hat{u}'(k,l,0)\,\mathrm{sign}\left[\frac{m(z)}{m(0)}\right]\left|\frac{m(z)}{m(0)}\right|^{1/2} \times \exp\left[i\int_0^z m(z)\,dz\right], \tag{4}$$

$$\hat{v}'(k,l,z) = \hat{v}'(k,l,0)\,\mathrm{sign}\left[\frac{m(z)}{m(0)}\right]\left|\frac{m(z)}{m(0)}\right|^{1/2} \times \exp\left[i\int_0^z m(z)\,dz\right]. \tag{5}$$

Orographic gravity waves excited by an isolated or complex orography can always be represented by a spectrum of wavenumbers, whose direction and amplitude depend on the bottom boundary condition [as shown by (2)]. Hence, the wave equation has to be solved for each wavenumber and, in physical space, the resulting wave pattern will be given by the Fourier integral (or sum) of their contributions (Nappo 2012).

From the equations shown above it can be seen that, in directional shear flows, the mountain wave equation [(1)] becomes singular at critical levels, where $\boldsymbol{\kappa}_H \cdot \mathbf{U} = ku_0 + lv_0 = 0$. For a wavenumber approaching its critical level, m approaches infinity according to (3), and the Fourier transform of the vertical velocity $\hat{w}$ becomes small ($\hat{w} \to 0$) according to (2). On the other hand, according to (4) and (5), the Fourier transform of the horizontal velocity perturbation diverges [$(\hat{u}', \hat{v}') \to \infty$] (Shutts 1998). The net result is an increase of the wave amplitude in the vicinity of a critical level. However, only wavenumbers with large spectral amplitudes approaching critical levels will in practice contribute to wave breaking (since this process is intrinsically defined in physical space) and the subsequent generation of turbulence; small-amplitude wavenumbers will be absorbed at the critical levels, as described by linear theory (Booker and Bretherton 1967). Note also that the products of $\hat{u}'$ and $\hat{w}$, and of $\hat{v}'$ and $\hat{w}$, remain finite near critical levels [as shown by (2), (4), and (5)], despite the divergence of $\hat{u}'$ and $\hat{v}'$, since their amplification cancels out with the attenuation of $\hat{w}$. These products would in fact be exactly constant with height if there were no singularities in the integrals in the exponents of (2), (4), and (5), which account for the absorbing effect of critical levels (cf. Broad 1995; Teixeira and Miranda 2009).

The diagnosis of critical levels induced by directional wind shear can only be made in Fourier space (where the orientation and the amplitude of each wavenumber may be determined), as explained above, but it is the wave energy distribution by wavenumber in the wave spectrum that ultimately determines whether wave breaking occurs or not.

3. Methodology

a. *PIREPs and case study selection*

Pilot reports (PIREPs) of turbulence were used to select cases where atmospheric turbulence was reported, in the presence of directional wind shear, over the Rocky Mountains. An accurate description of the PIREPs database used here is provided by Wolff and Sharman (2008). In the same paper, those authors discuss generic issues and limitations of using pilot reports as a research tool (see also Schwartz 1996). Here, we recall that while PIREPs represent a reliable method to determine turbulence occurrence, the information they provide about time, location, and turbulence intensity

may not be accurate. More specifically, Sharman et al. (2006) showed that, on average, the uncertainty associated with pilot reports is 50 km along the horizontal direction, 200 s in time, and 70 m along the vertical direction. Despite this uncertainty, pilot reports have been conveniently employed in studies aimed at evaluating/validating turbulence occurrence (Kim and Chun 2010; Trier et al. 2012; Ágústsson and Ólafsson 2014; Keller et al. 2015) for lack of a better alternative.

In this paper, PIREPs are used to identify days where generic atmospheric turbulence, or MWT, was reported by pilots over the Rocky Mountains in the state of Colorado. In particular, moderate or severe turbulence reports within the upper troposphere (from 4 km to the tropopause height) are considered. The lowest 4 km of the atmosphere were excluded to eliminate low-level turbulence and directional wind shear associated with boundary layer processes. Note that the highest mountain peak considered here is about 4 km (above sea level), and the boundary layer height over mountainous terrain is expected to adjust to the terrain elevation following the topography, so exclusion of the lowest 4 km should avoid the boundary layer almost completely (DeWekker and Kossmann 2015).

The analysis focused on the winter seasons of 2 years of data: 2015 and 2016. Climatologies of mountain-wave activity (Julian and Julian 1969; Wolff and Sharman 2008) show that this activity is larger over the Rocky Mountains during the winter months, when low-level winds are strong and westerly (i.e., perpendicular to the dominant mountain ridges). Furthermore, the stronger jet stream in winter favors the existence of both speed and directional wind shear via the thermal wind relation. The atmospheric conditions were evaluated using soundings measured upstream of the Rocky Mountains. The meteorological station selected was Grand Junction, Colorado (Fig. 1), and the data were downloaded from the website of the University of Wyoming (http://weather.uwyo.edu/upperair/sounding.html). In Fig. 2 the wind speed and direction, as well as the atmospheric stability (quantified through the squared Brunt–Väisälä frequency N^2) are shown at 0000 UTC 7 February 2015. This day was chosen as a case study because of the fairly continuous change of wind direction with height and a tropopause height of about 11 km. The existence of a high tropopause facilitates excluding the stability change with height taking place in its vicinity from the possible mechanisms causing wave breaking and, thus, responsible for the turbulence encounters reported in the first 10 km of the atmosphere (further indications that this is plausible are given below). As can be seen in Fig. 2, the rate of wind turning with height is not constant but varies from a maximum of $50^\circ\,\mathrm{km}^{-1}$ at lower levels (up to 4 km) and $10^\circ\,\mathrm{km}^{-1}$ at higher altitudes (6–8 km), to a slower rotation rate (between 3° and $5^\circ\,\mathrm{km}^{-1}$) in the atmospheric layers between 4 and 6 km and above 10 km, respectively. The stronger wind turning existing in the lowest few kilometers of the atmosphere is expected, being probably due to boundary layer processes.

Figure 1b shows the location of the turbulence reports associated with the atmospheric conditions presented in Fig. 2. These reports were issued between 2 h before and 1 h after 0000 UTC 7 February 2015. Table 1 provides details about the turbulence encounters such as type, altitude, time of occurrence, intensity of the turbulence, and the cubic root of the eddy dissipation rate $\varepsilon^{1/3}$ (a standard measure of CAT) estimated from onboard data (Sharman et al. 2014).

b. Numerical simulations

The selected day was investigated by performing semi-idealized numerical simulations using the WRF-ARW atmospheric model (Skamarock and Klemp 2008). In this paper, by "semi-idealized simulations" we mean simulations performed by running the WRF Model in an idealized setup, but using as input data real orography (truncated as explained next) and a real atmospheric profile. Note that, as discussed in the introduction, the aim of the present paper is to assess whether the ingredients necessary for triggering mountain-wave breaking in the presence of directional wind shear existed for the atmospheric (and lower boundary) conditions under consideration. Therefore, this study does not attempt to simulate the full complexity of the flow on 7 February 2015 and of the associated turbulence events, for which detailed 3D weather fields and simulations with full physics (i.e., including a range of parameterizations) should be run.

The simulations used the model's dynamical core only (i.e., no parameterizations), and the flow was assumed to be adiabatic (no heat or moisture fluxes from the surface) and inviscid (no explicit diffusion and no planetary boundary layer). Furthermore, the Coriolis force was neglected (these two latter choices are justified below). The top of the model domain was at 25 km, and a 7-km-deep Rayleigh damping layer was used to control wave reflection from the upper boundary.

An isotropic horizontal grid spacing of $\Delta x = \Delta y = 1$ km was used, and the model's vertical grid comprised 100 stretched eta levels, corresponding (approximately) to equally spaced z levels ($\Delta z = 250$ m). With this resolution, we can expect the dominant mountain waves to be sufficiently well resolved by the model. Indeed, the dominant vertical wavelength of the gravity waves launched by the Rocky Mountains may be estimated using a 2D hydrostatic approximation as $\lambda_z \approx 2\pi U/N \approx 6$ km, if we take as a representative values $N = 0.01\,\mathrm{s}^{-1}$ and $U = 10\,\mathrm{m\,s}^{-1}$.

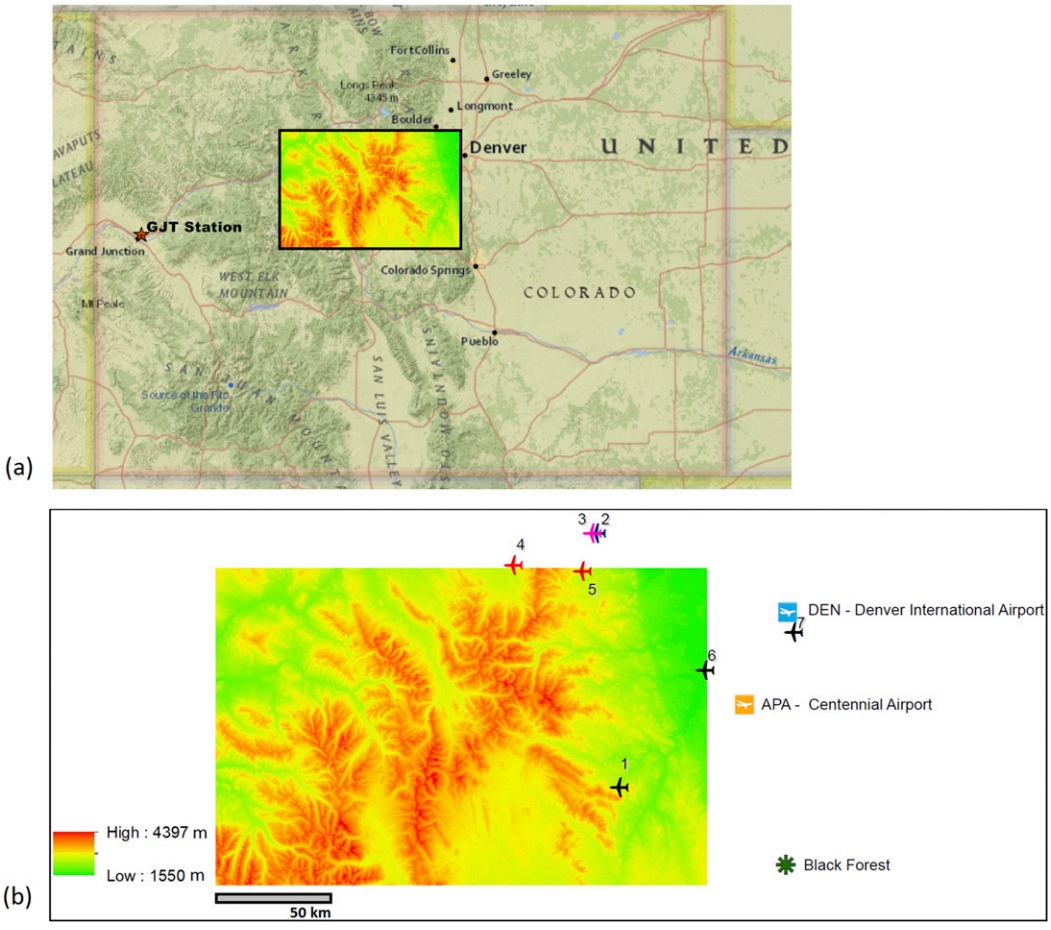

FIG. 1. (a) Map of the study area showing the Rocky Mountains in the state of Colorado and the location of the Grand Junction meteorological station (GJT). The highlighted rectangular area corresponds to the portion of the Rocky Mountains used as lower boundary condition for the semi-idealized runs (but not to the simulation domain, which is somewhat larger). (b) The location of the turbulence reports possibly related to the atmospheric conditions present at 0000 UTC 7 Feb 2015, as described in Table 1, and surrounding landmarks. The numbered aircraft symbols correspond to the turbulence reports' IDs in Table 1, the different colors are black for ModT, red for SevT, blue for ModMWT, and pink for SevMWT. The map only shows the portion of the Rocky Mountains used in the semi-idealized runs. Note that the black outline is only used to delimit the figure and does not correspond to the simulation domain.

The choice of a representative background wind speed is difficult, as will be discussed in more detail in section 4 (test 3), because the wind speed varies between 7 and 16 m s^{-1} in the lowest 3 km of the atmosphere. Even considering the lowest and highest values in the range of wind speed variation, which correspond to $\lambda_z \approx 4$ and 10 km, respectively, we can still expect to resolve the dominant mountain waves extremely well. Since from linear theory, in directional shear flows the vertical wavelength of wave components with critical levels becomes indefinitely small, the vertical resolution might be a more serious limitation than suggested by these rough estimates. However, because wave breaking happens in physical space and this singular behavior at critical levels occurs in spectral space, a range of scales is actually involved in a given wave breaking event. The numerical simulations of Guarino et al. (2016) (using a comparable vertical resolution) suggest that such resolutions are sufficient to capture the smallest scales in flow overturning regions (see their Fig. 5).

Each model simulation lasted 10 h and model outputs were stored every 15 min. Because of the idealized model configuration and the relatively small domain used (see below), a spinup time of 1 h was found to be sufficient for sound waves to leave the computational domain (their speed is ≈1000 km h^{-1}) and for a quasi-stationary mountain-wave field to be established.

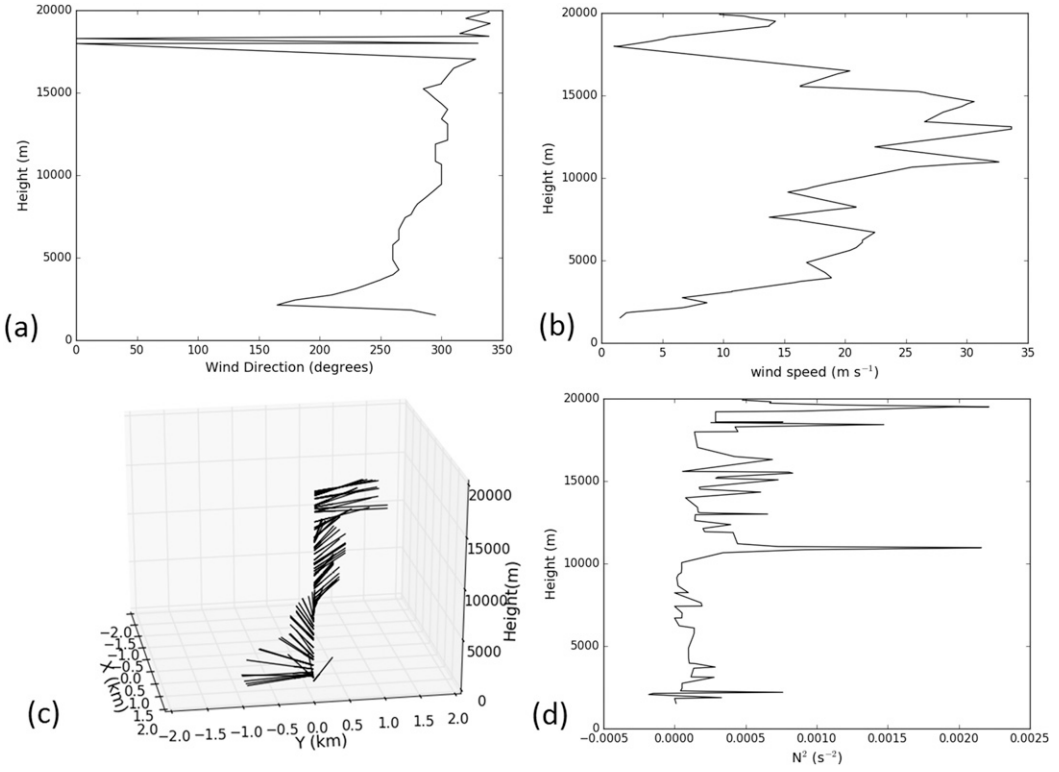

FIG. 2. Variation of the (a) wind direction, (b) wind speed, and (d) squared Brunt–Väisälä frequency N^2 with height for 0000 UTC 7 Feb 2015. The meteorological data come from the Grand Junction station, located upstream of the Rocky Mountains (station elevation: 1475 m) (see Fig. 1). (c) The variation of the wind direction with height, but using vectors with a constant length to represent the turning wind profile. Note that the vectors point toward the vertical axis in the middle.

The model was initialized using the wind profile and the atmospheric stability profile shown in Fig. 2. A portion of the Rocky Mountains range (the rectangular area in Fig. 1), downstream of the Grand Junction meteorological station (for the predominant flow direction), with a (zonal) length of 223 km and a (meridional) width of 144 km was chosen as the lower boundary condition. The terrain elevation data come from the U.S. Geological Survey's 1-arc-s resolution national elevation dataset (NED), resampled to 1 km. Open lateral boundary conditions were used. The real orography was placed approximately in the middle of the computational domain in order to avoid steep terrain at the lateral boundaries. Numerical instability arising from high vertical velocities as the incoming flow moves from flat to steep terrain was avoided by applying a smoothing along the edges of the topography. In particular, 10 grid points were used to smooth the terrain elevation departing from the edge of the topography. The total size of the simulation domain is 400 km × 400 km.

Although by choosing such a large mountainous region as a forcing the effects of the Coriolis force on the

TABLE 1. Details about the turbulence reports, namely, ID, type [moderate or severe turbulence (ModT and SevT, respectively), moderate or severe mountain-wave turbulence (ModMWT and SevMWT, respectively)], time, altitude, and intensity of the turbulence, as well as the cubic root of the eddy dissipation rate $\varepsilon^{1/3}$. Note that 1 ft = 0.03048 m.

ID	Type of turbulence	Time and date	Altitude (ft)	$\varepsilon^{1/3}$ (m$^{2/3}$ s^{-1})
1	ModT	2241 UTC 6 Feb 2015	24 000	0.50
2	ModMWT	2257 UTC 6 Feb 2015	22 000	0.50
3	SevMWT	2259 UTC 6 Feb 2015	24 000	0.62
4	SevT	2347 UTC 6 Feb 2015	24 000	0.75
5	SevT	0115 UTC 7 Feb 2015	16 000	0.75
6	ModT	0115 UTC 7 Feb 2015	13 000	0.50
7	ModT	0115 UTC 7 Feb 2015	20 000	0.50

dynamics of mountain waves may become important ($af/U \gtrsim 1$, where a is a characteristic mountain half-width, f is the Coriolis parameter, and U is a velocity scale for the background wind), in this study rotation effects are neglected (by imposing $f = 0$). The ambiguous definition of mountain width in this case with complex terrain makes af/U difficult to estimate. The value of af/U is much less than 1 if calculated taking into account a typical value for the width of single peaks in the mountain range [i.e., $a = 10$ km, following Doyle et al. (2000)], but on the contrary, it is large and of order 1 if calculated considering the mountainous region as a whole (i.e., $a \approx 100$ km).

To assess to what extent the presence of Earth's rotation can influence the generation and propagation of mountain waves, a simulation in which the Coriolis force was allowed to act on the flow perturbations was run. Although some discrepancies were found between the two experiments with and without Earth's rotation, the overall flow pattern and, most importantly, the location of flow instability regions were only marginally affected. This in principle means that for our purposes the effect of the small-scale individual mountains is dominant, and that for the semi-idealized simulations presented here rotation effects are nearly negligible.

The neglect of diffusion implied by not using a turbulence closure aims to address an initially laminar state of the atmosphere from which turbulence arises as a consequence of static and dynamic instabilities caused by wave steepening and breaking. Neglecting the planetary boundary layer (PBL) may seem a radical approach, but additional simulations (not shown) using the Yonsei University (YSU) PBL parameterization showed that results did not change appreciably. Although the regions of flow instability were confined to a smaller region, they occupied essentially the same positions in space and were characterized by similar values of the Richardson number. An advantage of inviscid simulations is that they avoid the uncertainty associated with PBL parameterizations, which are known to be especially questionable over mountainous terrain (DeWekker and Kossmann 2015).

The model setup described above was used for all performed simulations, including the sensitivity tests presented in the next section. Variations made to this initial configuration for each sensitivity test (i.e., changes in the orography, wind, and stability profiles) will be described in the results section that follows.

4. Results and discussion

a. *Semi-idealized simulations: Real atmospheric sounding and orography*

Instabilities generated within the computational domain were detected by looking at fields such as the potential temperature, the magnitude of the wave horizontal velocity perturbation vector (u', v'), and the Richardson number of the total flow including the wave perturbation $\mathrm{Ri}_{\mathrm{out}}$. The Richardson number was calculated at each model grid point using centered finite differences. Because the model vertical resolution is such that mountain waves are sufficiently well resolved (see section 3b for details), the Ri field is expected to be well resolved, too. Indeed, because of the idealized nature of the simulations presented here, mountain-wave propagation and breaking are the only reason for the modulation of Ri. Note that since the simulations are inviscid, and thus no turbulence parameterizations are used, $\mathrm{Ri}_{\mathrm{out}}$ values of less than 0.25 and/or 0 are used to detect dynamical ($\mathrm{Ri}_{\mathrm{out}} < 0.25$) and convective ($\mathrm{Ri}_{\mathrm{out}} < 0$) instability regions that can potentially evolve into turbulence. $\mathrm{Ri}_{\mathrm{out}}$ values from inviscid simulations provide information on how close the flow can get to instability, without being affected by the parameterized turbulent mixing that would immediately act to restore the flow stability and neutralize layers with $N^2 < 0$.

Figure 3a shows the grid points in the computational domain where $\mathrm{Ri}_{\mathrm{out}}$ is lower than 0.25. The $\mathrm{Ri}_{\mathrm{out}} \leq 0.25$ field was computed between 4 and 18 km, which corresponds (approximately) to the region between the height of the highest mountain peak and the height of the sponge layer employed in the simulations. The first 4 km of the atmosphere were excluded from the analysis because of unrealistic atmosphere–ground interactions that develop in frictionless simulations, leading to low Ri values just above the ground (Guarino et al. 2016). As shown in Fig. 3a, low Ri values occur just above the mountain peaks (in relation, perhaps, to the aforementioned atmosphere–ground interactions), between 6.5- and 10-km heights and between 15- and 18-km heights. While the highest-level instabilities occur in the stratosphere and therefore no pilot reports are available for validation purposes (aircraft cruise altitudes are usually up to about 12 km), the region of low Ri values located between 6.5 and 10 km shows good agreement with the PIREPs database. Indeed, most of the turbulence reports indicate turbulence occurrence between 6 and 7.5 km (see Table 1).

In Fig. 4a contours of negative values of $\mathrm{Ri}_{\mathrm{out}}$ (indicating flow overturning) at $z \approx 7.5$ km are shown. The background field is the terrain elevation. It can be seen that the location of the wave breaking event between 6- and 7.5-km heights, mentioned above, agrees well with the turbulence report 1 marked in Fig. 1b (ModT 1 in Table 1), both in the vertical and horizontal directions.

In sections 4b and 4c, attention will be focused on analyzing to what extent directional wind shear is primarily responsible for the wave breaking event displayed in Fig. 4a (note that at different simulation times and at different locations we can observe more wave breaking

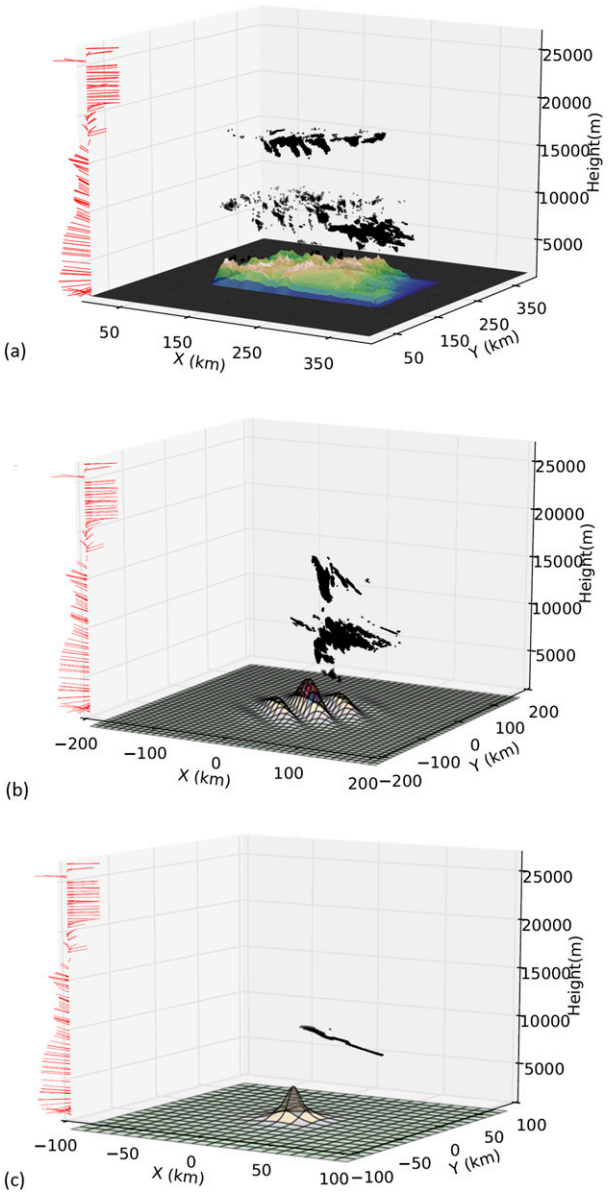

FIG. 3. 3D plots showing every point in the computational domain where $Ri_{out} \leq 0.25$ for the three simulations performed with a real input sounding and (a) a real orography, (b) an idealized mountain ridge, and (c) a bell-shaped mountain (test 1). In (a) the Ri_{out} field contains flow-overturning regions where $Ri_{out} < 0$, and the simulation time shown is $t = 105$ min. In (b) and (c) the simulation time shown is $t = 360$ min; however, in (c) the Ri_{out} field is never negative (at any simulation time).

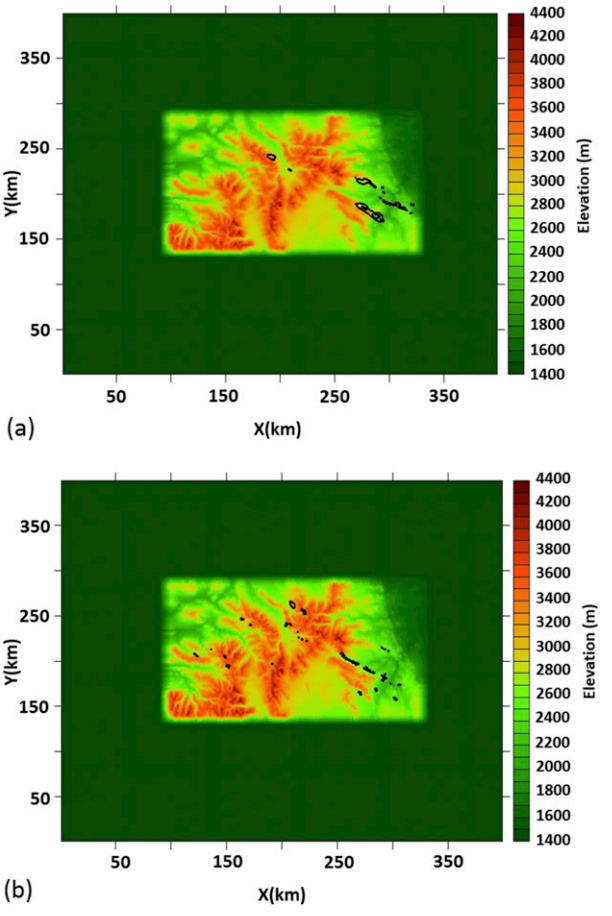

FIG. 4. Horizontal cross sections of the $Ri_{out} < 0$ field at $z \approx 7.5$ km, at the simulation time $t = 105$ min. (a) The real input sounding containing both speed and directional wind shear, and (b) the modified input sounding, where only directional wind shear is present (test 3). The background field is the terrain elevation.

events; however, as the availability of PIREPs is dictated by the flight routes, there are no turbulence reports directly linkable to those events).

b. *Sensitivity tests*

Despite the simplicity of the semi-idealized simulations performed, wave breaking events detected in the simulation domain cannot be automatically associated with the presence of directional wind shear. Indeed, at least three other possible environmental conditions able to modulate the gravity wave amplitude can be identified: 1) a sufficiently high or steep orography; 2) the variation of N with height, in particular at the tropopause; and 3) the speed shear in the wind profile. Sensitivity tests were performed to investigate the role of each of these physical mechanisms separately. Note that the unsteady nature of the flow in a wave breaking event makes comparisons between the simulations more difficult, since the evolution of two flows can be similar but asynchronous. The results presented next were analyzed through the use of animations of the studied quantities over time, and the snapshots presented in this paper are representative of the overall flow features detected.

1) TEST 1: THE BOTTOM BOUNDARY CONDITION/ SURFACE FORCING

The mechanism responsible for wave breaking in directional shear flows is sensitive to the bottom boundary condition [as shown by (2)], which may play a crucial role in the wave breaking process. We can hypothesize that orographies with different shapes, heights, and orientations will excite waves with high energy at wavenumbers that have critical levels at different heights, or will interact with a given critical level (i.e., at a similar height) in a different way, depending on the spectral energy distribution [see section 2, or Guarino et al. (2016) for a more extended discussion].

To test the role of the lower boundary condition, two simulations with the same realistic input sounding presented in section 3 but idealized orographies were run. More specifically, the first sensitivity test was performed using an axisymmetric bell-shaped mountain given by

$$h(x,y) = \frac{H}{\left(\frac{x^2}{a^2} + \frac{y^2}{a^2} + 1\right)^{3/2}}, \tag{6}$$

where, following Doyle et al. (2000), the mountain height is $H = 2$ km and its half-width is $a = 10$ km, which are typical values for the Colorado Front Range (Doyle et al. 2000). Note that a mountain height of 2 km is consistent with the mountain prominence relative to the surrounding terrain as seen by the incoming flow in the realistic orography simulation, because the Grand Junction station used to initialize the model is located at about 1.5 km above sea level. Unlike Doyle et al. (2000), who modeled the Rocky Mountains using an idealized 2D ridge, in this experiment a 3D mountain is adopted. While it could be argued that a two-dimensional representation of the Rocky Mountains would provide a more realistic approximation to their large-scale structure, here we are interested in how the smaller-scale structure, which is intrinsically 3D, affects wave breaking, via fulfilment of the $\mathbf{U} \cdot \boldsymbol{\kappa}_H = 0$ condition. In the case of a (perfect) 2D orography with $l = 0$ the definition of critical level reduces to the one valid in unidirectional flows. However, the realistic orography considered here will certainly excite waves with wavenumber vectors spanning various directions (i.e., $l \neq 0$), so use of a 3D idealized mountain is justified. Furthermore, the horizontal propagation of 3D mountain waves affect the wave amplitude, and thus the likeliness of wave breaking and turbulence occurrence, as discussed in Eckermann et al. (2015) and Xu et al. (2017).

For the second sensitivity test, an idealized 3D mountain ridge containing a few peaks (Martin and Lott 2007) was used:

$$h(x,y) = \frac{H}{2}\exp\{-[(x/a_{\mathrm{rdg}})^2 + (y/a_{\mathrm{rdg}})^2]\} \times [1 + \cos(k_s x + l_s y)], \tag{7}$$

where the height of the highest peak in the mountain ridge is $H = 2$ km; the characteristic horizontal length scale of the orography envelope is $a_{\mathrm{rdg}} = 50$ km; and l_s and l_s, the horizontal wavenumbers of the smaller-scale orography, have been chosen so that the half-width of each peak (defined as the horizontal distance from the peak where the terrain elevation is half its maximum) is 10 km. From visual inspection, this reproduces reasonably well the dominant smaller scales present in the real orography. The orography profile defined using the above parameters extends over an area of approximately 180 km × 130 km, is oriented northwest–southeast and contains five peaks (see Fig. 3b).

Although still drastically idealized, this orography approximates better the surface forcing imposed by the Rocky Mountains in terms of spatial extent (the fraction of the Rocky Mountains considered in this study extends over an area of about 220 km × 150 km), the ridges' orientation (in particular of those peaks near which turbulence was observed, according to turbulence report 1), and introduces a range of scales that attempts to (partially) reproduce the many smaller-scale features of the real orography. Using this approach, the interaction between different wavenumbers excited by the orography can be taken into account.

In Figs. 3b and 3c the $\mathrm{Ri}_{\mathrm{out}} \leq 0.25$ field obtained for the two idealized orography simulations is shown and compared to that obtained for the real orography simulation (Fig. 3a). When an isolated mountain is used (Fig. 3c), despite the idealized simulation setup, the model is able to reproduce the occurrence of dynamical instabilities at higher levels in the atmosphere but fails to predict the true location of the observed instability region. Indeed, most of the turbulence reports indicate turbulence between 6 and 7.5 km (Table 1) while, in this simulation, instabilities take place in a thin layer between ≈9.3 and 10 km. Furthermore, taking a closer look at the $\mathrm{Ri}_{\mathrm{out}}$ field reveals that no negative $\mathrm{Ri}_{\mathrm{out}}$ values exist, so no flow overturning caused by wave breaking is taking place in the simulation domain. However, when a mountain ridge with a few peaks is used (Fig. 3b) the instability region is wider and more pronounced, contains negative $\mathrm{Ri}_{\mathrm{out}}$ values and, most importantly, resembles better the flow simulated using the real orography (Fig. 3a). Flow instabilities occur at lower levels (≈4 km), between 7.5 and 11.5 km (showing a better agreement with the observations), and also at higher altitudes (≈14.5–16.5 km).

We can conclude that there is overall a poor agreement between these idealized simulations and the PIREPs, but significant improvements are observed when an orography profile with a few peaks is considered. This is a consequence of the fact that, although we still retain some elements needed to generate mountain waves that may break in directional wind shear (viz., a stably stratified atmosphere, representative values of mountain height and width, and a wind direction that changes with height), the wave solution obviously depends on the Fourier transform of the terrain elevation $\hat{h}(k, l)$ [see (2)]. Hence, the energy associated with each wavenumber excited at the surface is closely linked to the shape and orientation of the mountain profile. Consequently, the wave spectrum excited by an axisymmetric mountain, or an idealized mountain range, and by the realistic orography are quite different and the interaction between wavenumbers and directional critical levels differs accordingly.

2) TEST 2: THE TROPOPAUSE AND THE VARIATION OF N WITH HEIGHT

Previous studies (Worthington 1998; Whiteway et al. 2003; McHugh and Sharman 2013) pointed out how the interaction between vertically propagating orographic waves and the tropopause may trigger wave breaking and thus high-level turbulence generation. Furthermore, inhomogeneities in the atmospheric stability can cause wave reflection (Queney 1947) that, by constructive or destructive interferences between upward- and downward-propagating waves, can modulate the surface drag and the wave amplitude itself (Leutbecher 2001). Similar wave modulations and modifications of the wave breaking conditions may be produced by sharp vertical variations in the background flow shear (Teixeira and Miranda 2005).

Although the investigated turbulence encounter was reported at a height of about 7.3 km, and therefore it is quite distant from the tropopause (in Fig. 2c a substantial increase in N^2 that may be identified as the tropopause occurs at about 11 km), a simulation without the tropopause, more specifically, assuming a constant $N = 0.01\,\mathrm{s}^{-1}$, was run. The aim of this simulation was to exclude as a possible cause for wave breaking the existence of significant wave reflections that could potentially take place not only because of the high value of N at the tropopause itself, but also because of the variation of N within the troposphere. This latter effect might also lead to substantial modulation of the wave amplitude by refraction [according to (2), (4), and (5)].

In Fig. 5 vertical (west–east) cross sections of the magnitude of the wave horizontal velocity perturbation vector (u', v') are shown. The cross sections pass through the grid point where turbulence was reported (Y = 180 km in Fig. 4a), and the black contours delimit the regions where $\mathrm{Ri}_{\mathrm{out}}$ is negative. Figure 5a refers to the real sounding simulation and Fig. 5b to the simulation with a constant N. The studied wave breaking event, responsible for the negative $\mathrm{Ri}_{\mathrm{out}}$ values between 6.5 and 10 km, is present in both simulations. Although in Fig. 5b the instability regions are smaller, they present the same wake structure (discussed later in this section) visible in Fig. 5a where patches of negative $\mathrm{Ri}_{\mathrm{out}}$ propagate downstream. Also, at the same height, the (u', v') magnitude has a very similar pattern (and value) in both flows.

This result indicates that wave reflection is probably not significant enough to cause wave breaking. However, the large stability jump at the tropopause cannot be ignored, and wave reflection is still expected to occur to some degree. An estimation of how much reflection should be expected for the stability profile in Fig. 2b can be obtained by calculating the reflection coefficient $R = (N_2 - N_1/N_2 + N_1)$, proposed by Leutbecher (2001) for 2D flows, where we omit the minus sign included by Leutbecher to make R positive. This expression for R is valid for waves traveling in layers with constant N_1 and N_2. Since in the sounding of Fig. 2b, N^2 varies substantially, the values of N_1 and N_2 adopted here must be understood as averages below and above the large N maximum that corresponds to the tropopause, respectively. Taking $N_1 = 0.01\,\mathrm{s}^{-1}$ at $z = 10$ km and $N_2 = 0.02\,\mathrm{s}^{-1}$ at $z = 11.2$ km, we note that these are quite typical values for the troposphere and stratosphere and correspond to $R = 1/3$. Therefore, we can expect that about one-third of the upward-propagating mountain waves be reflected back at the tropopause. However, in order for this reflection to cause wave enhancement, the phase of the reflected wave must also be properly tuned (Leutbecher 2001). The N maximum at the tropopause could also lead to horizontally propagating waves trapped at that height (Teixeira et al. 2017), but since those waves decay exponentially in the vertical, their effect at $z \approx 6$–7 km should be relatively modest. Hence, consistent with Fig. 5b, these do not seem to be the dominant mechanisms causing wave breaking.

The analysis presented above suggests that the effects of the tropopause and of the N variation in general do not play an important role in causing the observed turbulence and, thus, are not of key relevance to the event under investigation.

3) TEST 3: THE SPEED SHEAR

Alongside the variation of N with height, the change of wind speed with height represents an additional

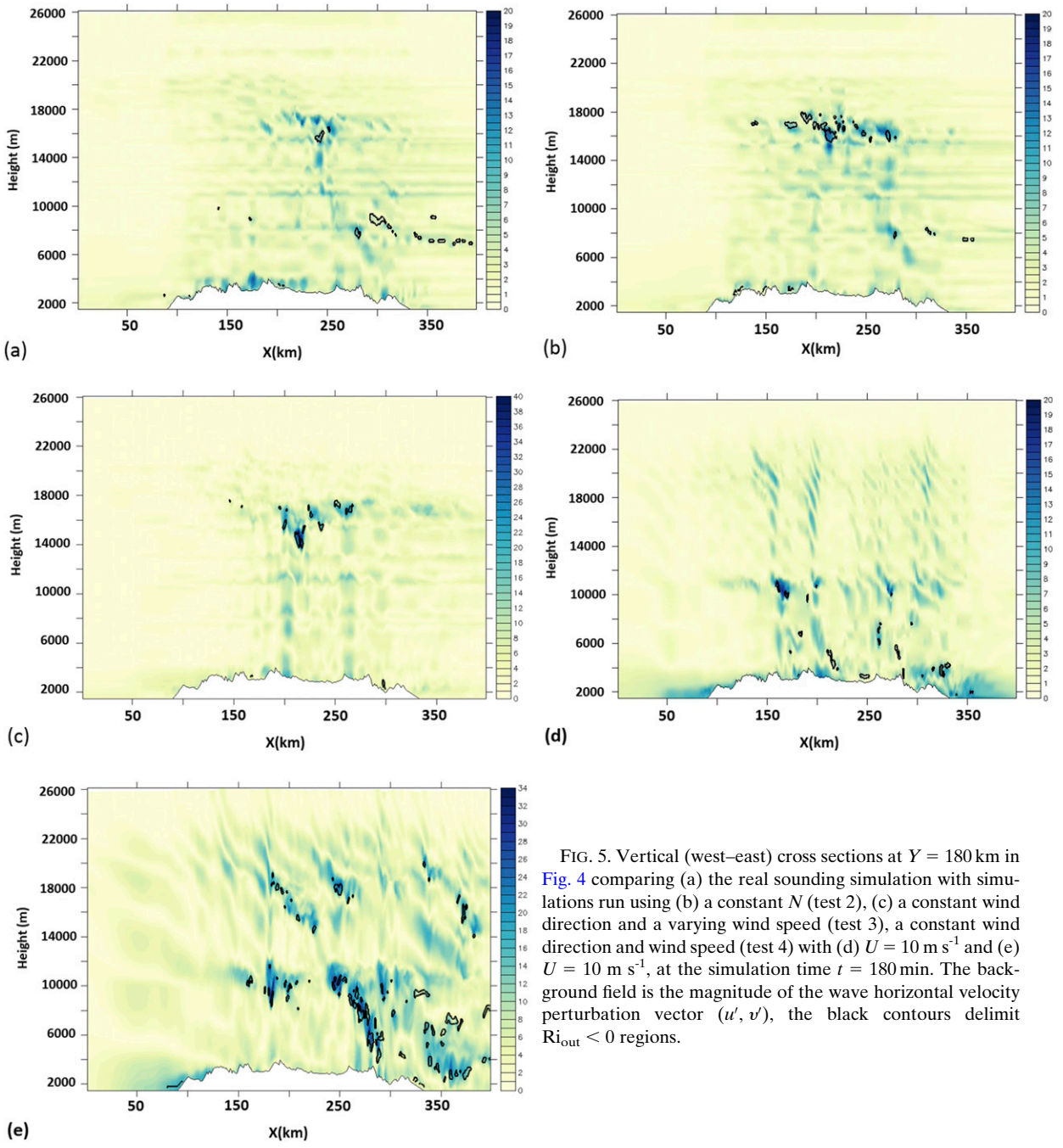

FIG. 5. Vertical (west–east) cross sections at $Y = 180$ km in Fig. 4 comparing (a) the real sounding simulation with simulations run using (b) a constant N (test 2), (c) a constant wind direction and a varying wind speed (test 3), a constant wind direction and wind speed (test 4) with (d) $U = 10\ \mathrm{m\ s^{-1}}$ and (e) $U = 10\ \mathrm{m\ s^{-1}}$, at the simulation time $t = 180$ min. The background field is the magnitude of the wave horizontal velocity perturbation vector (u', v'), the black contours delimit $\mathrm{Ri_{out}} < 0$ regions.

factor able to modulate the amplitude of gravity waves [see (2), (4), and (5)]. In particular, it is known [and consistent with (4) and (5)] that a decreasing wind speed with height represents the best condition for wave steepening (Smith 1977; McFarlane 1987; Sharman et al. 2012), which can facilitate the breaking of already-large-amplitude waves. As can be seen in Fig. 2b, overall, the speed shear is positive over most of the troposphere, where the wind speed tends to increase with height; however, regions where the wind speed decreases with height are also present.

The speed shear contribution was eliminated by modifying the input wind profile so that the u and v components varied with height accounting only for the observed change in the wind direction, neglecting the variation caused by the changes in wind speed, which was kept fixed at $10\ \mathrm{m\ s^{-1}}$. The large wind speed variation for the specific day under consideration did not

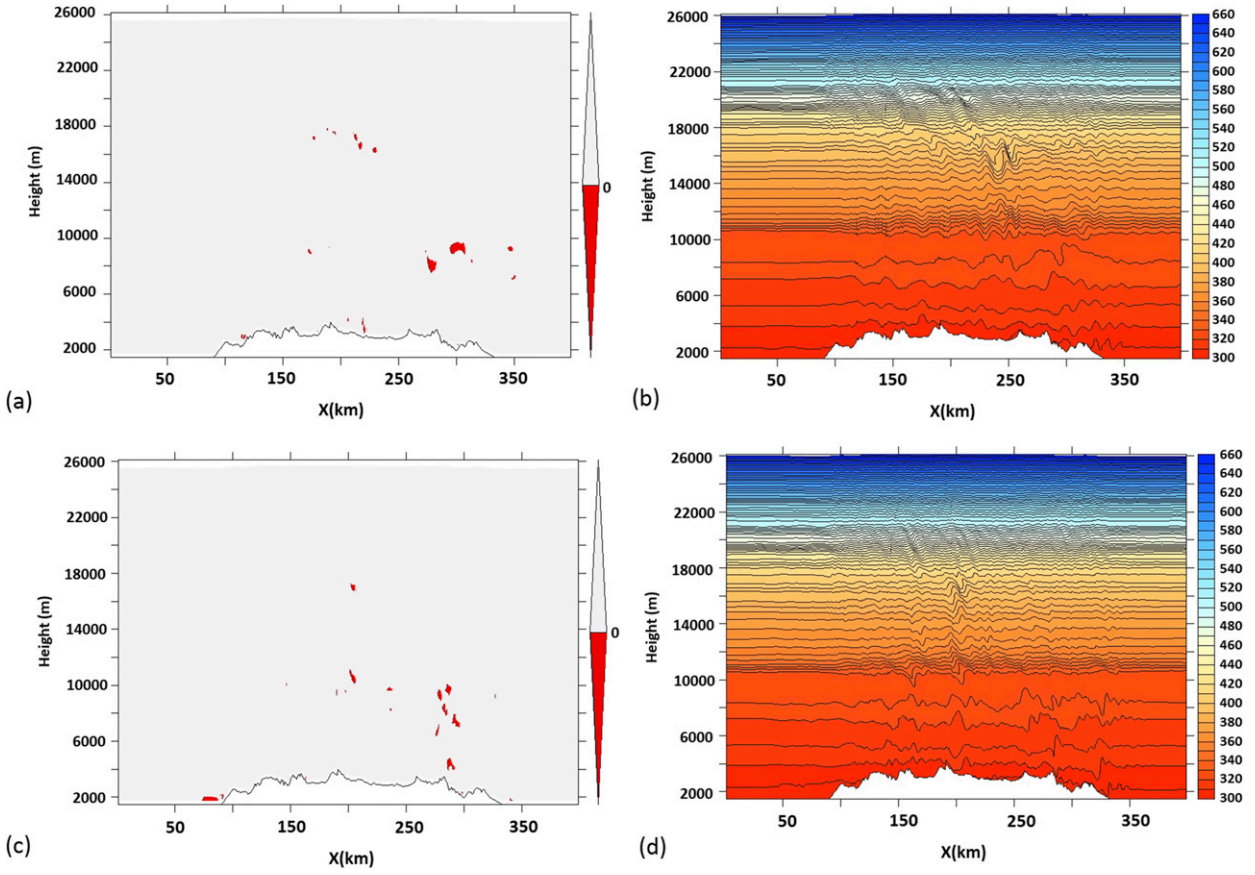

FIG. 6. Vertical (west–east) cross sections of regions where (a),(c) $Ri_{out} < 0$ and of (b),(d) potential temperature fields passing through the point where turbulence was reported ($Y = 180$ km in Fig. 4) at the simulation time $t = 135$ min, with (a) and (b) corresponding to the simulation with the real input sounding and (c) and (d) corresponding to the simulation where speed shear was neglected (test 3).

make it easy to identify a dominant wind speed. Indeed, while the wind speed of the flow crossing the mountain between 2.2- and 3.6-km altitude varies in the range 7–16 m s^{-1}, the wind speed over the mountain peaks is about 20 m s^{-1}. The value 10 m s^{-1} was chosen because it approximates better the wind speed at low levels, which is presumably responsible for generating the waves (see also test 4, in the following section, where this assumption is further tested).

In Fig. 4b the $Ri_{out} < 0$ field at $z \approx 7.5$ km for the new simulation including only directional wind shear is shown. Both in Fig. 4a (the real sounding simulation) and Fig. 4b overturning regions with approximately the same location and having the same elongated shape are visible. Figures 6a and 6b show again contours of negative values of Ri_{out} in west–east vertical cross sections passing through the point where turbulence was reported ($Y = 180$ km in Fig. 4a). Figure 6a corresponds to the simulation with the real input sounding, and Fig. 6c corresponds to the simulation without speed shear. Figures 6b and 6d show the same comparison but for the potential temperature fields. From Fig. 6 we can see that the wave breaking region occurs in the two simulations at similar altitudes (between 6 and 10 km).

Despite some differences between the two simulations (note that by modifying the input sounding we are modifying the background state in which the waves are generated), the occurrence of wave breaking does not seem to be related to the presence of speed shear.

A second test was performed to further assess the speed shear contribution to wave breaking. The input wind profile was again modified but this time the u and v components varied with height accounting only for the observed wind speed variation, and the directional wind shear was eliminated by using a constant wind direction (chosen as a "dominant wind direction" taken by inspection of the atmospheric sounding in Fig. 2a as 260°).

In Figs. 5a and 5c vertical cross sections for the real sounding simulation (Fig. 5a) and the speed shear–only simulation (Fig. 5c) are shown. The background field is the magnitude of the horizontal velocity perturbation vector (u', v'), and the black contours delimit the region

with $Ri_{out} < 0$. In Fig. 5a waves break at an altitude of about 7 km, as discussed in section 4a. When directional wind shear is removed (Fig. 5c) no overturning regions where $Ri_{out} < 0$ are observed within the troposphere (and lower stratosphere). However, in the speed shear–only simulation, wave breaking at $z \approx 15$–17 km is intensified and here the magnitude of the (u', v') vector increases up to 40 m s^{-1}.

The atmospheric sounding in Fig. 2b shows a net decrease of the wind speed with height in the layer between 14 and 18 km. This significant negative wind shear is probably responsible for the high-altitude wave breaking. In the absence of directional wind shear, the filtering of the waves at lower levels is removed and all the wavenumbers in the wave spectrum break at essentially the same height. Thus, the wave energy is dissipated in a thin layer, rather than over the entire troposphere, resulting in the larger velocity perturbations observed in Fig. 5c.

4) TEST 4: THE MOUNTAIN-WAVE AMPLITUDE

A last test was necessary to verify our hypothesis that waves are breaking because of critical levels imposed by the variation of the wind direction with height, and not only because of a highly nonlinear boundary condition such as is imposed by the Rocky Mountains. Indeed, for NH/U values larger than 1, linear theory breaks down and wave breaking is expected to occur even in unsheared flows (Huppert and Miles 1969; Smith 1980; Miranda and James 1992).

For this purpose, simulations in which both wind speed and direction are kept constant were performed. In these simulations the wind direction was again set to 260° and we used two different values of wind speed: $U =$ 10 and 20 m s^{-1}. As discussed in the previous section, the choice of a representative wind speed of the flow passing over the orography is difficult because of the large variation of U in the lowest 3.5 km of the atmosphere. In the sensitivity tests presented here, 10 m s^{-1} was used because it was assumed to be representative of the flow at lower levels, while 20 m s^{-1} was used to test the robustness of this assumption, and also because it is the wind speed just above the highest mountain peaks.

Figure 5d compares the $U = 10$ m s^{-1} simulation with the real sounding simulation of Fig. 5a. While in Fig. 5a the breaking region is again easily detected between 7 and 10 km, where patches of negative values of the Richardson number appear, for the simulation with a constant wind speed and direction (Fig. 5d), the waves continue to propagate upward without breaking at the same heights and horizontal locations.

This ability of the gravity waves to propagate to higher levels in the atmosphere supports the argument that, by removing the directional wind shear, we removed the mechanism responsible for wave breaking in the event under consideration (this test also directly compares with test 3, Fig. 4b, where $U = 10$ m s^{-1} and directional wind shear is present). More specifically, without directional wind shear, the filtering of the wave energy by critical levels vanishes. Therefore, wavenumbers that would otherwise be absorbed into the mean flow, or increase their amplitude and cause wave breaking, remain essentially unaffected and keep on propagating upward.

In addition to vertically propagating gravity waves, in Fig. 5d, a few instability regions are also visible, but not at the correct levels. The mechanism behind these instabilities, and the associated wave breaking, can only be related to the high amplitude of the surface forcing provided by the Rocky Mountains, conjugated with the decrease of density with height (which are the only possible wave breaking mechanisms active in this case).

When $U = 20$ m s^{-1} is assumed (Fig. 5e), large-amplitude gravity waves are excited by the Rocky Mountains that break vigorously [the maximum on the $|(u', v')|$ scale is 34 m s^{-1}] both at lower and higher atmospheric levels.

The opposite flow behavior observed in the two tests is a consequence of the transition between two well-known different flow regimes. Assuming $N = 0.01$ s^{-1} and $H = 2$ km, which is a good estimate of the mountain height as seen by the incoming flow (the Grand Junction station used to initialize the model is located at about 1.5 km above sea level), $NH/U = 2$ when $U = 10$ m s^{-1} and $NH/U = 1$ when U = 20 m s^{-1}. For a 3D orography, when $NH/U = 2$ the flow enters a "flow around" regime for which a significant part of the flow is deflected around the flanks of the obstacle and the generation of vertically propagating mountain waves is weakened. When $NH/U = 1$ most of the incoming flow passes over the orography and wave breaking is favored (Miranda and James 1992).

In reality, the amplitude of the waves excited by the Rocky Mountains will be the result of a varying wind speed, and not of a fixed U. Therefore, although the flow simulated using $U = 10$ m s^{-1} is closer to the one in Fig. 5a in terms of magnitude of the velocity perturbation vector, the wave breaking found when $U = 20$ m s^{-1} suggests that the effective wind speed of the flow approaching the mountain can be decisive in causing wave breaking. We conclude that it is not possible to exclude self-induced overturning from the possible wave breaking mechanisms. Instead, this mechanism is probably acting alongside the directional wind shear mechanism (as discussed in more detail in the following section).

c. The directional wind shear contribution

While tests 2, 3, and 4 investigated the role of static stability, speed shear, and mountain-wave amplitude in causing the studied turbulence encounter, in this section more direct evidence that waves may break because of environmental critical levels associated with the presence of the directional wind shear will be presented and discussed.

Both in the horizontal cross section of Fig. 4 and in the vertical cross section of Fig. 5a, the region corresponding to $\mathrm{Ri}_{\mathrm{out}} < 0$ exhibits an elongated shape that, departing from the first wave breaking point, extends downstream forming a certain (small) angle with the wind direction (which is very close to 270°) at that height. This downwind transport of statically unstable air seems to be a signature of breaking waves in directional shear flows. Based on linear theory arguments, Shutts (1998) demonstrated the existence of a flow feature known as "asymptotic wake" (see also Shutts and Gadian 1999). The asymptotic wake is a consequence of wavenumbers approaching critical levels in directional shear flows and, more precisely, of a component of the background wind parallel to the wave phase lines that will advect the wave energy away from the mountain (in stationary conditions).

The asymptotic wake predicted by Shutts translates into lobes of maximum wave velocity perturbation extending along the wind direction at each height, but not perfectly aligned with it (Fig. 7a). Steady linear theory predicts that shear will become indefinitely large in these flow regions. We speculate that the tail of negative Ri values in Figs. 4 and 5a, which is absent in all the breaking regions in test 4 (e.g., Fig. 5d), is a manifestation of the asymptotic wake predicted by Shutts (1998). Although the asymptotic wake is a feature of steady flow, it develops because of advection of the wave field by the wind at critical levels, which means that it can extend over long distances in short time intervals, even when the flow is not perfectly steady.

In Fig. 7 the magnitude of the horizontal velocity perturbation vector (u', v') is shown for five different cases:

- Figures 7a and 7b show the flow behavior for orographic waves excited by an axisymmetric mountain [as described by (6)] in the case of a background wind direction that changes (backs) continuously with height (constant rate of rotation $\approx 14°\ \mathrm{km}^{-1}$), a constant $N = 0.01\,\mathrm{s}^{-1}$, and wind speed $U = 10\,\mathrm{m\,s}^{-1}$. Figure 7a shows the analytical solution obtained from a linear model for such a flow, similar to that developed by Teixeira and Miranda (2009), in Fig. 7b the corresponding idealized numerical simulation (with $H = 1\,\mathrm{km}$) is presented. The numerical setup for this idealized simulation is slightly different from the one presented in section 3 [see Guarino et al. (2016) for further details].
- Figures 7c and 7d correspond to test 1, therefore they depict simulations that use an idealized 3D orography [as described by (6)] and a set of idealized mountain ridges [as described by (7)], but a real atmospheric sounding.
- Figure 7e corresponds to the semi-idealized simulation that uses real orography and a real atmospheric sounding (more specifically, it focuses on a portion of the entire simulation domain shown in Fig. 4a, starting at $X = 240\,\mathrm{km}$, $Y = 110\,\mathrm{km}$).

The black contours are the lowest $\mathrm{Ri}_{\mathrm{out}}$ values for each simulation. Note that although in Figs. 7a and 7b the wind rotates counterclockwise and in Figs. 7c–e it rotates clockwise, this only modifies the quadrants in which the wave energy is advected at different heights (and so where the maximum of the wave perturbation field is), and the two sets of results may be seen as essentially equivalent via mirror and rotation transformations. The purpose of Fig. 7 is to show the progressive transition of the asymptotic wake structure as the degree of realism of the flow increases. The asymmetry of the wave perturbation field is visible in both Figs. 7a and 7b, where the left-hand branch extends to the northwest, asymptotically approaching the wind direction at that height (this is the asymptotic wake). As we shift toward less idealized flows (Figs. 7c–e), this flow feature becomes less clear but it is still detectable (albeit mirrored).

Proving the existence of the asymptotic wake in real case studies is of a particular interest, since approximately hydrostatic mountain waves (such as the ones excited by the Rocky Mountains) are usually expected to break and cause turbulence just above the mountain peaks and not far downstream, but this is what seems to happen when an asymptotic wake is present (see in particular Fig. 5a).

SPECTRAL ANALYSIS OF THE WAVE FIELD

A final piece of evidence supporting the importance of critical levels caused by directional wind shear is provided by spectral analysis carried out on the magnitude of the (u', v') field. The quantity (u', v') was chosen because of the strong amplification of the horizontal velocity perturbations at critical levels (Guarino et al. 2016). This spectral analysis will be first presented for the fully idealized simulation (with an idealized axisymmetric orography and idealized atmospheric sounding) introduced in the previous section, and then for the more realistic case being investigated.

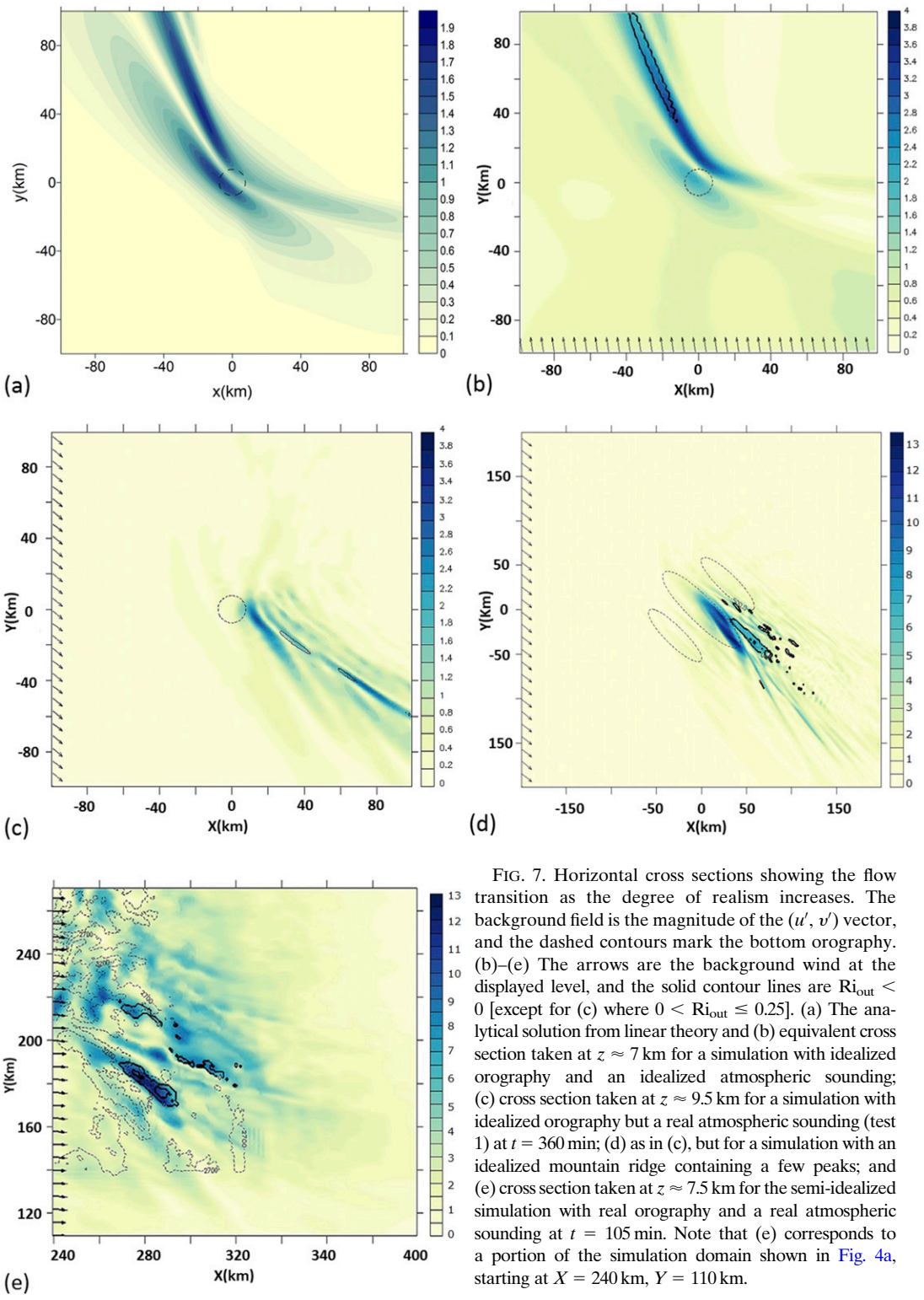

FIG. 7. Horizontal cross sections showing the flow transition as the degree of realism increases. The background field is the magnitude of the (u', v') vector, and the dashed contours mark the bottom orography. (b)–(e) The arrows are the background wind at the displayed level, and the solid contour lines are $\mathrm{Ri}_{\mathrm{out}} < 0$ [except for (c) where $0 < \mathrm{Ri}_{\mathrm{out}} \leq 0.25$]. (a) The analytical solution from linear theory and (b) equivalent cross section taken at $z \approx 7$ km for a simulation with idealized orography and an idealized atmospheric sounding; (c) cross section taken at $z \approx 9.5$ km for a simulation with idealized orography but a real atmospheric sounding (test 1) at $t = 360$ min; (d) as in (c), but for a simulation with an idealized mountain ridge containing a few peaks; and (e) cross section taken at $z \approx 7.5$ km for the semi-idealized simulation with real orography and a real atmospheric sounding at $t = 105$ min. Note that (e) corresponds to a portion of the simulation domain shown in Fig. 4a, starting at $X = 240$ km, $Y = 110$ km.

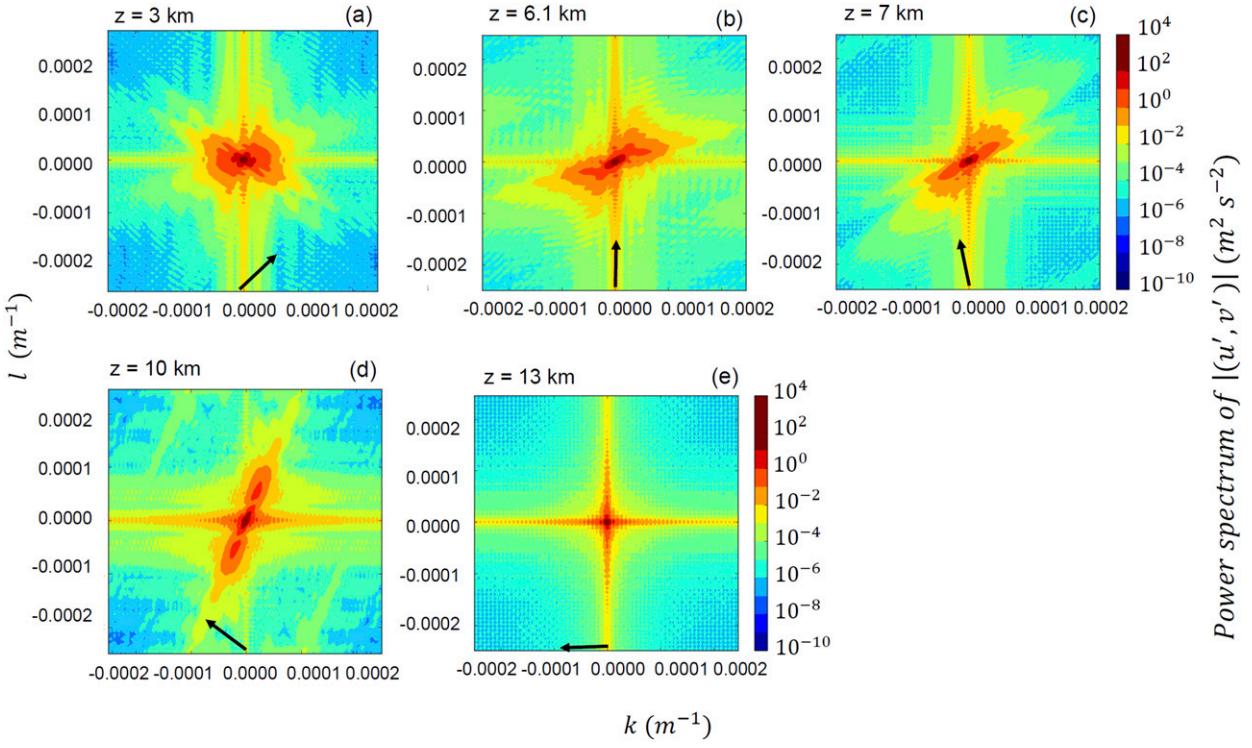

FIG. 8. 2D power spectra of the horizontal velocity perturbation field for an idealized numerical simulation of directional wind shear flow over an isolated axisymmetric mountain, computed at heights of (a) 3, (b) 6.1, (c) 7, (d) 10, and (e) 13 km. The axes show the wavenumber components along x and y. The black arrows indicate the wind direction at each height.

In Fig. 8[1] the 2D spatial power spectra of the horizontal velocity perturbation field, computed at different heights from the fully idealized simulation, are shown. The five spectra correspond to (u', v') horizontal cross sections taken at 3-, 6.1-, 7-, 10-, and 13-km heights, at a same simulation time. Note that Fig. 8c is the 2D power spectrum of Fig. 7b. Since the Fourier transform of a purely real signal is symmetric, in a 2D power spectrum all the information is contained in the first two quadrants of the (k, l) plane and the third ($k<0$, $l<0$) and fourth ($k>0$, $l<0$) quadrants are just mirrored images of the first ($k>0$, $l>0$) and second ($k<0$, $l>0$) quadrants, respectively.

For the idealized wind profile employed in this simulation, the continuous (and smooth) turning of the background wind vector with height creates a continuous distribution of critical levels in the vertical. At each critical level, the wave energy is absorbed into the background flow and this absorption affects one wavenumber in the spectrum at a time (i.e., at each level). Looking at the power spectra in Fig. 8, it can be seen that the dominant wavenumber at each height (i.e., that with most energy) is the one nearly perpendicular to the incoming wind (i.e., the one having a critical level at that height). As a consequence, the wavenumber vector of the most energetic wave mode rotates counterclockwise following the background wind, but about 90° out of phase. It can also be seen that as the incoming wind rotates by a certain angle, the portion of the wave spectrum corresponding to wavenumbers perpendicular to the wind at lower levels has been absorbed. For example, in Fig. 8b the wind is from the south, departing from a westerly surface direction, so all the wavenumbers in the second quadrant ($k<0$, $l>0$) have been absorbed. When the background wind has rotated by 180° (Fig. 8e) practically all the wave energy has been dissipated, because all possible critical levels have been encountered at lower altitudes (Teixeira and Miranda 2009) [this is confirmed by flow cross sections (not shown) where no waves exist above the height where the power spectrum in Fig. 8e was computed].

It should be noted that the angle actually detected between the background wind direction and the most energetic wave mode at each height is slightly less than

[1] Note that in both Figs. 8 and 9, the nonzero spectral energies extending along the x and y axes correspond to numerical noise generated in the computation of the 2D power spectra and so should be physically disregarded.

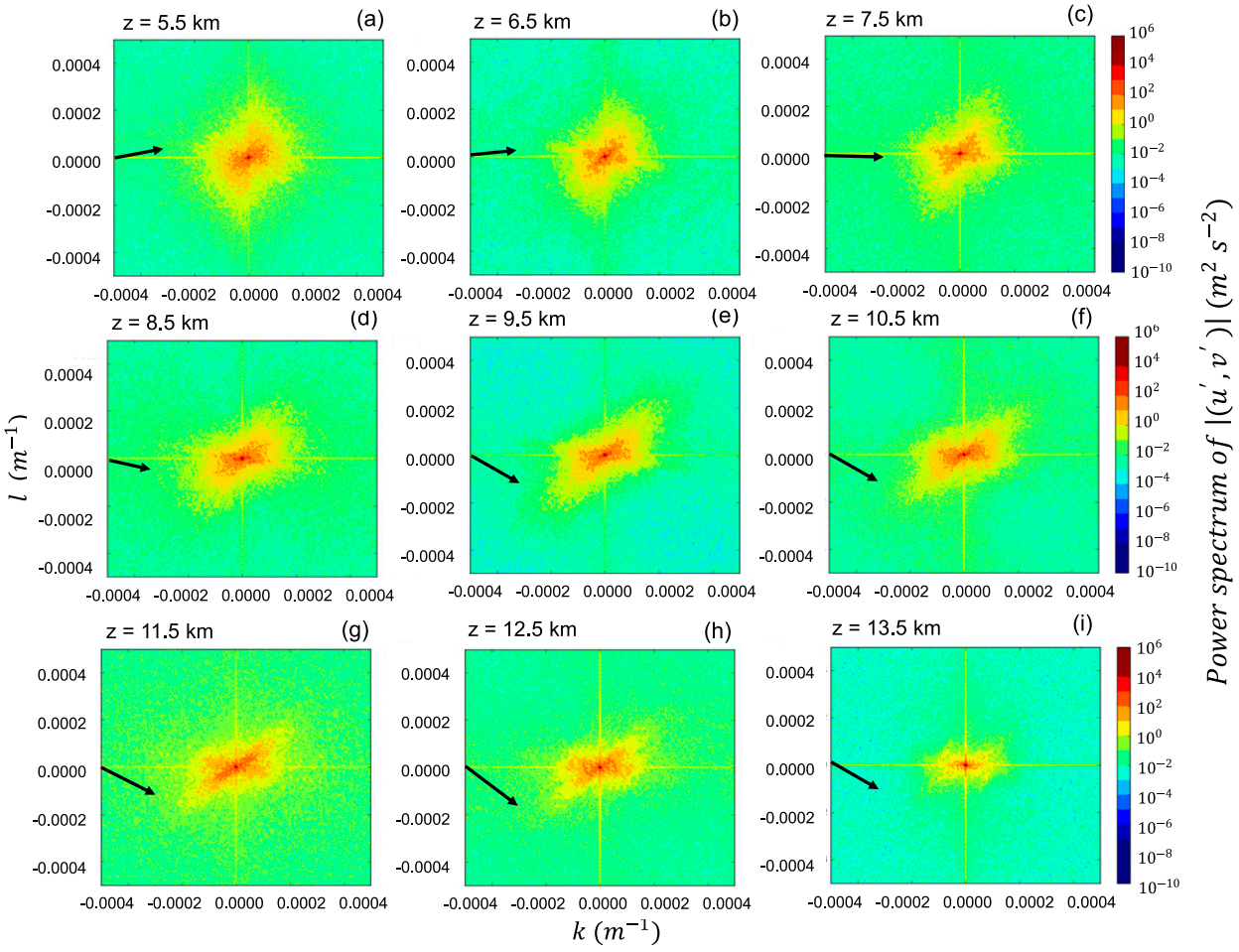

FIG. 9. 2D power spectra of the horizontal velocity perturbation field for the semi-idealized numerical simulation presented in section 4a, computed at heights corresponding to each kilometer of the atmosphere between 5.5 and 15.5 km. Axes and black arrows are as in Fig. 8.

90°. A plausible interpretation is that, although a wave reaches its maximum amplitude at a critical level in linear theory, this is also the height where it will break. For finite-amplitude waves, amplification and breaking tends to occur some distance below critical levels. Therefore, typically, the energy carried by a wavenumber vector perpendicular to the wind has already been absorbed, and so the angle between wavenumbers that still carry maximum energy (prior to breaking) and the local wind direction will be less than 90°. An estimate of this effect can be obtained as follows. Taking the wave amplitude at wave breaking altitude as ≈500 m (not shown) and multiplying this by the turning rate of the background wind ≈14° km^{-1}, a misalignment of ≈7° is obtained. This is at least on the same order of magnitude as the value that can be estimated visually from Fig. 8.

When similar 2D power spectra are computed for the more realistic case under consideration, significant similarities can be seen. In Fig. 9 the 2D spatial power spectra computed from the semi-idealized numerical simulation are shown at heights comprising every kilometer of the atmosphere between 5.5 and 15.5 km. Figure 9c is the 2D power spectrum of Fig. 7e. The slower and nonconstant rate of wind turning with height characterizing this case makes it more difficult to detect the rotation of the dominant wavenumber following the wind. However, a rotation is still revealed by the changing orientation with height of the dominant wave energy lobes in the plots. In particular, approximate perpendicularity between the wind direction and the dominant wavenumbers can be seen between 7.5 and 10.5 km. These are the heights where, in physical space, most of the wave breaking occurs. Between 9.5 and 10.5 km, the wind direction remains essentially constant. At higher altitudes, 11.5–13.5 km, the wind rotation rate slows down and, as a consequence, the differences between spectra become harder to distinguish. By 13.5 km, because of the wave breaking taking place below and the

ensuing critical-level absorption, most of the wave energy has been dissipated. Note that, just as in the idealized case of Fig. 8, when measured more precisely the angle between the incoming wind vector and the dominant wavenumber vector is seen to be slightly lower than 90° (e.g., Fig. 9g).

The wave behavior inferred from the spectra in Fig. 9, being essentially similar to that displayed in Fig. 8, is equally explained by the mechanism leading to wave breaking in directional shear flows. In contrast, similar 2D power spectra computed for test 4 (not shown), where the wind direction is constant with height, display no selective wave-energy absorption as a function of height.

A final note on the power spectra of Fig. 9 concerns the modulation of the wave amplitude by the variation with height of background flow parameters. The existence of additional processes contributing to the wave dynamics is deducible from the power spectra computed between 9.5 and 12.5 km. Above 9.5 km the rotation of the wind slows down significantly and so it seems unlikely that directional critical levels are the only reason for the high-energy regions in the spectra of Figs. 9f–h. This is probably a consequence of changes in other background flow parameters with height, such as stability and wind speed. It was shown in Fig. 2b that the wind speed between 5.5 and 9.5 km decreases from 20.6 to 18 m s^{-1}. As mentioned previously [see test 3 and (2), (4), and (5)], this type of variation can cause the wave amplitude to increase. Additionally, the significant increase in N^2 starting at about 11 km can cause wave reflections [see test 2 and (2), (4), and (5)], which might also result in an enhancement of the wave amplitude at lower atmospheric levels by resonance. Although sensitivity tests 2 and 3 indicate that these mechanisms are not strong enough to cause wave breaking, they may still be strong enough for their influence on the wave amplitude to be revealed in the power spectra of Fig. 9.

5. Summary and conclusions

In this paper, mountain-wave turbulence in the presence of directional vertical wind shear over the Rocky Mountains in the state of Colorado has been investigated. For the winter seasons of 2015 and 2016, days with a significant directional wind shear within the upper troposphere (from 4 km to the tropopause height) were identified by analyzing atmospheric soundings measured upstream of the Rocky Mountains at the Grand Junction, Colorado, meteorological station (GJT). Among these days, pilot reports (PIREPs) of turbulence encounters were used to select cases where moderate or severe turbulence events were reported.

A selected case was investigated by performing semi-idealized numerical simulations, and sensitivity tests, aimed at discerning the contribution of mountain wave breaking caused by directional wind shear in the observed turbulence event. In these simulations, the WRF-ARW Model was initialized with a 1D atmospheric sounding from Grand Junction and a real (but truncated) orography profile. The orography was modified in sensitivity test 1, and the atmospheric sounding was modified in sensitivity tests 2, 3, and 4.

For the simulation with a realistic atmospheric sounding and orography, low positive and negative Richardson number values (used to identify regions of flow instability) occurred between 6.5 and 10 km, providing overall good agreement with the PIREPs.

In test 1, the role of the surface forcing in causing wave breaking was investigated. In particular, the lower boundary condition was modified and replaced with a 3D bell-shaped mountain and an idealized orography containing a few ridges. For these experiments, overall the agreement between model-predicted instabilities and PIREPs degraded. However, a better representation of flow dynamical and convective instabilities was achieved when the orography with a few peaks was considered. The results of test 1 support the hypothesis that, in directional shear flows, by exciting substantially different wave spectra, orographies with different shapes, heights, and orientations can change the nature of the wave–critical-level interaction.

In test 2, the effect of the tropopause and of the vertical variation of N on wave breaking were tested. The real atmospheric stability profile was replaced with an idealized profile prescribed by imposing a constant $N = 0.01\,\mathrm{s}^{-1}$. Despite the constant stability, the investigated wave breaking event still occurred, and the flow cross sections showed essentially the same features observed in the real-sounding simulation.

In test 3, the influence of the variation of wind speed with height on wave steepening was explored. In a first test, the speed shear contribution was eliminated by modifying the atmospheric sounding so that changes in u' and v' were due to directional wind shear only, while the wind speed was kept constant at 10 m s^{-1}. In a second test, the directional wind shear contribution was eliminated by keeping the wind direction constant with height while the observed wind speed variation was retained. In the directional shear–only simulation, the investigated turbulence encounter was still present. In the speed shear–only simulation, no overturning regions were found in the simulation domain at $z \approx 7$ km, where the studied turbulence encounter occurred. These tests suggest that wave breaking was not likely attributable to the presence of speed shear.

In test 4, the highly nonlinear boundary condition imposed by the Rocky Mountains [for which $NH/U = O(1)$] was studied. Both wind speed and direction were kept constant with height, but two different wind speeds were used, namely: $U = 10$ and $20\,\mathrm{m\,s^{-1}}$. For the $10\,\mathrm{m\,s^{-1}}$ simulation, $NH/U = 2$, so mountain waves were relatively weak and propagated upward without breaking at the level where turbulence was observed. For the $20\,\mathrm{m\,s^{-1}}$ simulation, $NH/U = 1$ and mountain waves broke at multiple altitudes. These tests show that for the orography and flow configuration under investigation, wave breaking is quite sensitive to the wind speed of the incoming flow. The large variation of U in the lowest kilometers of the atmosphere does not allow us to exclude self-induced overturning as a possible wave breaking mechanism. Instead, this mechanism probably coexists with the directional wind shear, which acts to localize vertically the wave breaking regions.

In connection with the studied wave breaking event, a significant downwind transport of unstable air was detected in horizontal cross sections of the flow. This allows mountain-wave-induced turbulence to be found at large horizontal distances from the orography that generates the waves. A possible explanation for the observed flow pattern is the existence of an ''asymptotic wake,'' as predicted by Shutts (1998) using linear theory for waves approaching critical levels in directional shear flows. The asymptotic wake translates into lobes of maximum wave energy extending roughly along the wind direction at a particular height, but not perfectly aligned with the wind. This peculiar flow structure was displayed by the horizontal velocity perturbation field (u', v') in horizontal cross sections of the simulated flow.

Critical levels associated with directional wind shear were further investigated using spectral analysis of the magnitude of the (u', v') vector. This was done for a fully idealized flow and for the more realistic flow that is the main focus of the present paper. Power spectra of the horizontal velocity perturbation at different heights and changes in the corresponding wave energy distribution by wavenumber (i.e., wave energy absorption/enhancement) were analyzed.

For the fully idealized simulation, the continuous distribution of critical levels in the vertical makes the dominant wavenumber vector at each height be (almost) perpendicular to the background wind vector at that height. As a result, the wavenumber vector of the most energetic wave mode rotates counterclockwise, following the background wind 90° out of phase. The implications of this for the approximate perpendicularity between the background wind vector and the wave velocity perturbation vector at critical levels is discussed by Guarino et al. (2016). For the semi-idealized simulation, it was still possible to detect a rotation of the dominant wavenumber with the wind, even if less clearly than in the idealized case. In particular, the wind direction and the dominant wavenumber were seen to be approximately perpendicular between 7.5 and 10.5 km where most of the wave breaking occurs in physical space.

The experiments discussed in this paper suggest that critical levels induced by directional wind shear played a crucial role in originating the investigated turbulence encounter (ModT 1 in Table 1). The directional wind shear contribution to wave breaking dynamics is particularly relevant to the problem of how the wave energy is selectively absorbed or dissipated at critical levels, which also has implications for drag parameterization (Teixeira and Yu 2014). Furthermore, directional wind shear produces regions of flow instability far downwind from the obstacle generating the waves. This is a nontrivial result, especially for hydrostatic mountain waves, which are expected to propagate essentially vertically, and are therefore treated in drag parameterizations using a single-column approach. This downstream propagation of instabilities, which is a manifestation of the ''asymptotic wake'' predicted by Shutts (1998), hence, represents an overlooked turbulence generation mechanism that, if adequately taken in account, might improve the location accuracy of mountain-wave turbulence forecasts.

The semi-idealized approach used here was particularly well suited to the aims of the present study, as it allowed us to isolate and investigate separately different wave breaking mechanisms. However, the simplifications adopted in the numerical simulations constitute a source of uncertainty regarding the applicability of the results to real situations. Making the numerical simulations more realistic by including missing physical processes (e.g., boundary layer effects, moisture, and phase transitions), would therefore be a natural next step to further understand the observed turbulence event.

Acknowledgments. M.V.G. and M.A.C.T. acknowledge the financial support of the European Commission under Marie Curie Career Integration Grant GLIMFLO, Contract PCIG13-GA-2013-618016. The National Center for Atmospheric Research is sponsored by the National Science Foundation.

REFERENCES

Ágústsson, H., and H. Ólafsson, 2014: Simulations of observed lee waves and rotor turbulence. *Mon. Wea. Rev.*, **142**, 832–849, https://doi.org/10.1175/MWR-D-13-00212.1.

Booker, J. R., and F. P. Bretherton, 1967: The critical layer for internal gravity waves in a shear flow. *J. Fluid Mech.*, **27**, 513–539, https://doi.org/10.1017/S0022112067000515.

Broad, A. S., 1995: Linear theory of momentum fluxes in 3-d flows with turning of the mean wind with height. *Quart. J. Roy. Meteor. Soc.*, **121**, 1891–1902, https://doi.org/10.1002/qj.49712152806.

Broutman, D., S. D. Eckermann, H. Knight, and J. Ma, 2017: A stationary phase solution for mountain waves with application to mesospheric mountain waves generated by Auckland Island. *J. Geophys. Res. Atmos.*, **122**, 699–711, https://doi.org/10.1002/2016JD025699.

Carslaw, K. S., and Coauthors, 1998: Increased stratospheric ozone depletion due to mountain-induced atmospheric waves. *Nature*, **391**, 675–678, https://doi.org/10.1038/35589.

DeWekker, S. F. J., and M. Kossmann, 2015: Convective boundary layer heights over mountainous terrain—A review of concepts. *Front. Earth Sci.*, **3**, 77, https://doi.org/10.3389/feart.2015.00077.

Dörnbrack, A., T. Gerz, and U. Schumann, 1995: Turbulent breaking of overturning gravity waves below a critical level. *Appl. Sci. Res.*, **54**, 163–176, https://doi.org/10.1007/BF00849114.

Doyle, J. D., and Q. Jiang, 2006: Observations and numerical simulations of mountain waves in the presence of directional wind shear. *Quart. J. Roy. Meteor. Soc.*, **132**, 1877–1905, https://doi.org/10.1256/qj.05.140.

Doyle, J., and Coauthors, 2000: An intercomparison of model-predicted wave breaking for the 11 January 1972 Boulder windstorm. *Mon. Wea. Rev.*, **128**, 901–914, https://doi.org/10.1175/1520-0493(2000)128<0901:AIOMPW>2.0.CO;2.

Durran, D. R., 1990: Mountain waves and downslope winds. *Atmospheric Processes over Complex Terrain*, W. Blumen, Ed., Springer, 59–81.

Eckermann, S. D., A. Dörnbrack, H. Flentje, S. B. Vosper, M. Mahoney, T. P. Bui, and K. S. Carslaw, 2006: Mountain wave–induced polar stratospheric cloud forecasts for aircraft science flights during SOLVE/THESEO 2000. *Wea. Forecasting*, **21**, 42–68, https://doi.org/10.1175/WAF901.1.

——, J. Ma, and D. Broutman, 2015: Effects of horizontal geometrical spreading on the parameterization of orographic gravity wave drag. Part I: Numerical transform solutions. *J. Atmos. Sci.*, **72**, 2330–2347, https://doi.org/10.1175/JAS-D-14-0147.1.

Elvidge, A. D., S. B. Vosper, H. Wells, J. C. Cheung, S. H. Derbyshire, and D. Turp, 2017: Moving towards a wave-resolved approach to forecasting mountain wave induced clear air turbulence. *Meteor. Appl.*, **24**, 540–550, https://doi.org/10.1002/met.1656.

Gill, P. G., 2014: Objective verification of world area forecast centre clear air turbulence forecasts. *Meteor. Appl.*, **21**, 3–11, https://doi.org/10.1002/met.1288.

——, and A. J. Stirling, 2013: Including convection in global turbulence forecasts. *Meteor. Appl.*, **20**, 107–114, https://doi.org/10.1002/met.1315.

Grubišić, V., and P. K. Smolarkiewicz, 1997: The effect of critical levels on 3D orographic flows: Linear regime. *J. Atmos. Sci.*, **54**, 1943–1960, https://doi.org/10.1175/1520-0469(1997)054<1943:TEOCLO>2.0.CO;2.

——, S. Serafin, L. Strauss, S. J. Haimov, J. R. French, and L. D. Oolman, 2015: Wave-induced boundary layer separation in the lee of the Medicine Bow Mountains. Part II: Numerical modeling. *J. Atmos. Sci.*, **72**, 4865–4884, https://doi.org/10.1175/JAS-D-14-0381.1.

Guarino, M.-V., M. A. C. Teixeira, and M. H. P. Ambaum, 2016: Turbulence generation by mountain wave breaking in flows with directional wind shear. *Quart. J. Roy. Meteor. Soc.*, **142**, 2715–2726, https://doi.org/10.1002/qj.2862.

Huppert, H. E., and J. W. Miles, 1969: Lee waves in a stratified flow. Part 3: Semi-elliptical obstacle. *J. Fluid Mech.*, **35**, 481–496, https://doi.org/10.1017/S0022112069001236.

Jiang, Q., and J. D. Doyle, 2004: Gravity wave breaking over the central Alps: Role of complex terrain. *J. Atmos. Sci.*, **61**, 2249–2266, https://doi.org/10.1175/1520-0469(2004)061<2249:GWBOTC>2.0.CO;2.

Julian, L. T., and P. R. Julian, 1969: Boulder's winds. *Weatherwise*, **22**, 108–126, https://doi.org/10.1080/00431672.1969.9932856.

Keller, T. L., S. B. Trier, W. D. Hall, R. D. Sharman, M. Xu, and Y. Liu, 2015: Lee waves associated with a commercial jetliner accident at Denver International Airport. *J. Appl. Meteor. Climatol.*, **54**, 1373–1392, https://doi.org/10.1175/JAMC-D-14-0270.1.

Kim, J.-H., and H.-Y. Chun, 2010: A numerical study of clear-air turbulence (CAT) encounters over South Korea on 2 April 2007. *J. Appl. Meteor. Climatol.*, **49**, 2381–2403, https://doi.org/10.1175/2010JAMC2449.1.

Kirshbaum, D. J., G. H. Bryan, R. Rotunno, and D. R. Durran, 2007: The triggering of orographic rainbands by small-scale topography. *J. Atmos. Sci.*, **64**, 1530–1549, https://doi.org/10.1175/JAS3924.1.

Lane, T. P., J. D. Doyle, R. D. Sharman, M. A. Shapiro, and C. D. Watson, 2009: Statistics and dynamics of aircraft encounters of turbulence over Greenland. *Mon. Wea. Rev.*, **137**, 2687–2702, https://doi.org/10.1175/2009MWR2878.1.

Leutbecher, M., 2001: Surface pressure drag for hydrostatic two-layer flow over axisymmetric mountains. *J. Atmos. Sci.*, **58**, 797–807, https://doi.org/10.1175/1520-0469(2001)058<0797:SPDFHT>2.0.CO;2.

Lilly, D. K., 1978: A severe downslope windstorm and aircraft turbulence event induced by a mountain wave. *J. Atmos. Sci.*, **35**, 59–77, https://doi.org/10.1175/1520-0469(1978)035<0059:ASDWAA>2.0.CO;2.

——, and P. J. Kennedy, 1973: Observations of a stationary mountain wave and its associated momentum flux and energy dissipation. *J. Atmos. Sci.*, **30**, 1135–1152, https://doi.org/10.1175/1520-0469(1973)030<1135:OOASMW>2.0.CO;2.

Martin, A., and F. Lott, 2007: Synoptic responses to mountain gravity waves encountering directional critical levels. *J. Atmos. Sci.*, **64**, 828–848, https://doi.org/10.1175/JAS3873.1.

McFarlane, N. A., 1987: The effect of orographically excited gravity wave drag on the general circulation of the lower stratosphere and troposphere. *J. Atmos. Sci.*, **44**, 1775–1800, https://doi.org/10.1175/1520-0469(1987)044<1775:TEOOEG>2.0.CO;2.

McHugh, J., and R. Sharman, 2013: Generation of mountain wave-induced mean flows and turbulence near the tropopause. *Quart. J. Roy. Meteor. Soc.*, **139**, 1632–1642, https://doi.org/10.1002/qj.2035.

Miranda, P. M. A., and I. N. James, 1992: Non-linear three-dimensional effects on gravity-wave drag: Splitting flow and breaking waves. *Quart. J. Roy. Meteor. Soc.*, **118**, 1057–1081, https://doi.org/10.1002/qj.49711850803.

Nappo, C. J., 2012: *An Introduction to Atmospheric Gravity Waves*. 2nd ed. Academic Press, 400 pp.

Queney, P., 1947: *Theory of Perturbations in Stratified Currents with Applications to Air Flow over Mountain Barriers.* University of Chicago Press, 81 pp.

Schwartz, B., 1996: The quantitative use of PIREPs in developing aviation weather guidance products. *Wea. Forecasting*, **11**, 372–384, https://doi.org/10.1175/1520-0434(1996)011<0372:TQUOPI>2.0.CO;2.

Sharman, R. D., and J. M. Pearson, 2017: Prediction of energy dissipation rates for aviation turbulence. Part I: Forecasting nonconvective turbulence. *J. Appl. Meteor. Climatol.*, **56**, 317–337, https://doi.org/10.1175/JAMC-D-16-0205.1.

Sharman, R., C. Tebaldi, G. Wiener, and J. Wolff, 2006: An integrated approach to mid- and upper-level turbulence forecasting. *Wea. Forecasting*, **21**, 268–287, https://doi.org/10.1175/WAF924.1.

——, S. B. Trier, T. P. Lane, and J. D. Doyle, 2012: Sources and dynamics of turbulence in the upper troposphere and lower stratosphere: A review. *Geophys. Res. Lett.*, **39**, L12803, https://doi.org/10.1029/2012GL051996.

——, L. B. Cornman, G. Meymaris, J. Pearson, and T. Farrar, 2014: Description and derived climatologies of automated in situ eddy-dissipation-rate reports of atmospheric turbulence. *J. Appl. Meteor. Climatol.*, **53**, 1416–1432, https://doi.org/10.1175/JAMC-D-13-0329.1.

Shutts, G., 1995: Gravity-wave drag parametrization over complex terrain: The effect of critical-level absorption in directional wind-shear. *Quart. J. Roy. Meteor. Soc.*, **121**, 1005–1021, https://doi.org/10.1002/qj.49712152504.

——, 1998: Stationary gravity-wave structure in flows with directional wind shear. *Quart. J. Roy. Meteor. Soc.*, **124**, 1421–1442, https://doi.org/10.1002/qj.49712454905.

Shutts, G. J., and A. Gadian, 1999: Numerical simulations of orographic gravity waves in flows which back with height. *Quart. J. Roy. Meteor. Soc.*, **125**, 2743–2765, https://doi.org/10.1002/qj.49712555920.

Skamarock, W. C., and J. B. Klemp, 2008: A time-split nonhydrostatic atmospheric model for weather research and forecasting applications. *J. Comput. Phys.*, **227**, 3465–3485, https://doi.org/10.1016/j.jcp.2007.01.037.

Smith, R. B., 1977: The steepening of hydrostatic mountain waves. *J. Atmos. Sci.*, **34**, 1634–1654, https://doi.org/10.1175/1520-0469(1977)034<1634:TSOHMW>2.0.CO;2.

——, 1980: Linear theory of stratified hydrostatic flow past an isolated mountain. *Tellus*, **32**, 348–364, https://doi.org/10.3402/tellusa.v32i4.10590.

Strauss, L., S. Serafin, S. Haimov, and V. Grubišić, 2015: Turbulence in breaking mountain waves and atmospheric rotors estimated from airborne in situ and Doppler radar measurements. *Quart. J. Roy. Meteor. Soc.*, **141**, 3207–3225, https://doi.org/10.1002/qj.2604.

Teixeira, M. A. C., 2014: The physics of orographic gravity wave drag. *Front. Phys.*, **2**, 43, https://doi.org/10.3389/fphy.2014.00043.

——, and P. M. A. Miranda, 2005: Linear criteria for gravity-wave breaking in resonant stratified flow over a ridge. *Quart. J. Roy. Meteor. Soc.*, **131**, 1815–1820, https://doi.org/10.1256/qj.04.155.

——, and P. Miranda, 2009: On the momentum fluxes associated with mountain waves in directionally sheared flows. *J. Atmos. Sci.*, **66**, 3419–3433, https://doi.org/10.1175/2009JAS3065.1.

Teixeira, M., and C. L. Yu, 2014: The gravity wave momentum flux in hydrostatic flow with directional shear over elliptical mountains. *Eur. J. Mech.*, **47B**, 16–31, https://doi.org/10.1016/j.euromechflu.2014.02.004.

——, P. M. A. Miranda, and M. A. Valente, 2004: An analytical model of mountain wave drag for wind profiles with shear and curvature. *J. Atmos. Sci.*, **61**, 1040–1054, https://doi.org/10.1175/1520-0469(2004)061<1040:AAMOMW>2.0.CO;2.

——, ——, and J. L. Argaín, 2008: Mountain waves in two-layer sheared flows: Critical-level effects, wave reflection, and drag enhancement. *J. Atmos. Sci.*, **65**, 1912–1926, https://doi.org/10.1175/2007JAS2577.1.

——, A. Paci, and A. Belleudy, 2017: Drag produced by waves trapped at a density interface in nonhydrostatic flow over an axisymmetric hill. *J. Atmos. Sci.*, **74**, 1839–1857, https://doi.org/10.1175/JAS-D-16-0199.1.

Trier, S. B., R. D. Sharman, and T. P. Lane, 2012: Influences of moist convection on a cold-season outbreak of clear-air turbulence (CAT). *Mon. Wea. Rev.*, **140**, 2477–2496, https://doi.org/10.1175/MWR-D-11-00353.1.

Turner, J., 1999: Development of a mountain wave turbulence prediction scheme for civil aviation. Met Office Tech. Rep. 265, 34 pp.

Whiteway, J. A., E. G. Pavelin, R. Busen, J. Hacker, and S. Vosper, 2003: Airborne measurements of gravity wave breaking at the tropopause. *Geophys. Res. Lett.*, **30**, 2070, https://doi.org/10.1029/2003GL018207.

Wolff, J. K., and R. D. Sharman, 2008: Climatology of upper-level turbulence over the contiguous United States. *J. Appl. Meteor. Climatol.*, **47**, 2198–2214, https://doi.org/10.1175/2008JAMC1799.1.

Worthington, R. M., 1998: Tropopausal turbulence caused by the breaking of mountain waves. *J. Atmos. Sol.-Terr. Phys.*, **60**, 1543–1547, https://doi.org/10.1016/S1364-6826(98)00105-9.

Xu, X., Y. Wang, and M. Xue, 2012: Momentum flux and flux divergence of gravity waves in directional shear flows over three-dimensional mountains. *J. Atmos. Sci.*, **69**, 3733–3744, https://doi.org/10.1175/JAS-D-12-044.1.

——, J. Song, Y. Wang, and M. Xue, 2017: Quantifying the effect of horizontal propagation of three-dimensional mountain waves on the wave momentum flux using Gaussian beam approximation. *J. Atmos. Sci.*, **74**, 1783–1798, https://doi.org/10.1175/JAS-D-16-0275.1.